Supporting Information

Tetrathiafulvalene-based covalent organic framework as high-voltage organic cathodes for lithium batteries

Gonçalo Valente,[a] Raquel Dantas,[a] Pedro Ferreira,[a] Rebecca Grieco,[b] Nagaraj Patil,[b] Ana Guillem-Navajas,[c] David Rodríguez-San-Miguel,[c,d] Félix Zamora,[c,e] Roman Guntermann,[f] Thomas Bein,[f] João Rocha,[a] Helena Braga,[g,h] Karol Strutyński,[a] Manuel Melle-Franco,[a,*] Rebeca Marcilla,[b,*] Manuel Souto[a,i,*]

[a] Department of Chemistry, CICECO-Aveiro Institute of Materials, University of Aveiro, Aveiro, 3810-393, Portugal

[b] Electrochemical Processes Unit, IMDEA Energy Institute, Avda. Ramón de La Sagra 3, 28935 Móstoles, Spain

[c] Departamento de Química Inorgánica, Universidad Autónoma de Madrid, Madrid, 28049 Spain

[d] Institute for Advanced Research in Chemical Sciences (IAdChem), Universidad Autónoma de Madrid Campus de Cantoblanco, 28049 Madrid, Spain

[e] Condensed Matter Physics Center (IFIMAC), Universidad Autónoma de Madrid, 28049 Madrid, Spain

[f] Department of Chemistry and Center for NanoScience (CeNS), Ludwig-Maximilians-Universität München, Butenandtstraße 5-13 (E), 81377 Munich, Germany

[g] Engineering Physics Department, Engineering Faculty, University of Porto, 4200–465 Porto, Portugal

[h] MatER – Materials for Energy Research Laboratory, Engineering Faculty, University of Porto, Portugal

[i] CIQUS, Centro Singular de Investigación en Química Bioloxica e Materiais Moleculares, Departamento de Química-Física, Universidade de Santiago de Compostela, 15782, Santiago de Compostela, Spain

Contents

1. General methods and materials

All **reagents and solvents** employed in the syntheses were of high purity grade and were purchased from Sigma-Aldrich Co., TCI, or ChemExtension.

^{1}H liquid-state NMR spectra were recorded on a Bruker AVANCE 300 spectrometer (300 MHz). Tetramethylsilane (TMS) was used as an internal reference. Chemical shifts (δ) are quoted in ppm from TMS and the coupling constants (*J*) in Hz.

Fourier transform infrared (FTIR) spectra were recorded using powdered samples in an ATR FT-IR GALAXY SERIES FT-IR 7000 (Mattson Instruments) spectrometer in the 4000 – 400 cm^{-1} range.

^{13}C solid-state NMR spectra were recorded on a 9.4 T Bruker Avance III 400 spectrometer using a 4 mm Bruker magic-angle spinning (MAS) probe. Chemical shifts are quoted in ppm from TMS using solid adamantane as secondary references.

Powder X-ray diffraction (XRD) patterns were recorded using an Empyrean PANalytical diffractometer (Cu $K\alpha_{1,2}$ X-radiation, λ_1 = 1.540598 Å; λ_2 = 1.544426 Å), equipped with a PIXcel 1D detector and a flat-plate sample holder in a Bragg-Brentano para-focusing optics configuration (45 kV, 40 mA). The experimental patterns were fitted using Pawley refinement using GSAS-II software.

Thermogravimetric analysis (TGA) was carried out with a Shimadzu TGA 50 equipment in the 25–600 ºC temperature range under a 5 ºC min^{-1} scan rate and an N_2 flow of 20 $mL \cdot min^{-1}$.

The **UV-vis-NIR** absorption and diffuse reflectance spectra of the samples were measured using a Lambda 950 dual-beam spectrometer (PerkinElmer) and Reflectance FLEX Pack (Sarspec). The diffuse reflectance spectra are reported as the Kubelka-Munk transform, where $F(R) = (1-R)^2/2R$. The direct optical band gaps of these materials were determined from respective Tauc plots.

N_2 isotherms were collected at 77 K using a 3FLEX™ (Micromeritics). Before measurements, samples were outgassed at 393 K and 10^{-2} Torr overnight using a Smart VacPrep (Micromeritics) equipment. BET surface values were calculated from the N_2 isotherms using BETSI[1] and pore size distributions were obtained using the non-local density functional theory (NLDFT) method.

EPR measurements were performed in a Bruker ESP- 300E spectrometer operating in the X band 9.861 GHz and with a field modulation of 2 GHz at room temperature.

Scanning electron microscopy (SEM) and energy-dispersive X-ray spectroscopy (EDX) analysis were performed by using a JEOL JSM-7900F equipped with ULTIM Max 170 from Oxford Instruments.

The **electrochemical experiments** were performed using an Autolab electrochemical workstation (PGSTAT302N) using Nova 2.1 electrochemical software. A typical three-electrode experimental cell equipped with a platinum wire as the counter electrode and a silver wire as the pseudo-reference electrode was used for the electrochemical characterization of the working electrodes. The electrochemical properties were first studied by measuring the cyclic voltammogram at different scan rates in previously N_2 purged 0.1 M $TBAPF_6/CH_3CN$ solution. Ferrocene was added as an internal standard upon completion of each experiment. All potentials are reported in V versus Ag_{wire}. Working electrode preparation: The COF powdered materials (2 mg) were mixed in 2 mL of Nafion and ethanol (1:3 v/v). 100 µL of this dispersions were deposited on a 3 mm diameter glassy carbon disc working electrode, which was previously polished with 0.3, 0.1, and 0.05 µm alumina powders. Afterwards, the solvent was evaporated at room temperature.

Van der Pauw measurements were carried out using an ECOPIA Model HMS-5300 Hall measurement setup at room temperature (292 K). Gold contact electrodes were placed in a square geometry with distances of 2.4 mm on pressed pellets of the crystalline samples. Powder pellets were pressed by using approximately 20 mg of COF material and pressing it into a cylindrical pellet with a circle diameter of 1 cm under a pressure of 8 MPa. Pellet thicknesses were measured with a slide gauge to be about 200 µm.

2. Synthesis of TTF-COFs

2.1. Synthesis of TTF-Ph-COF

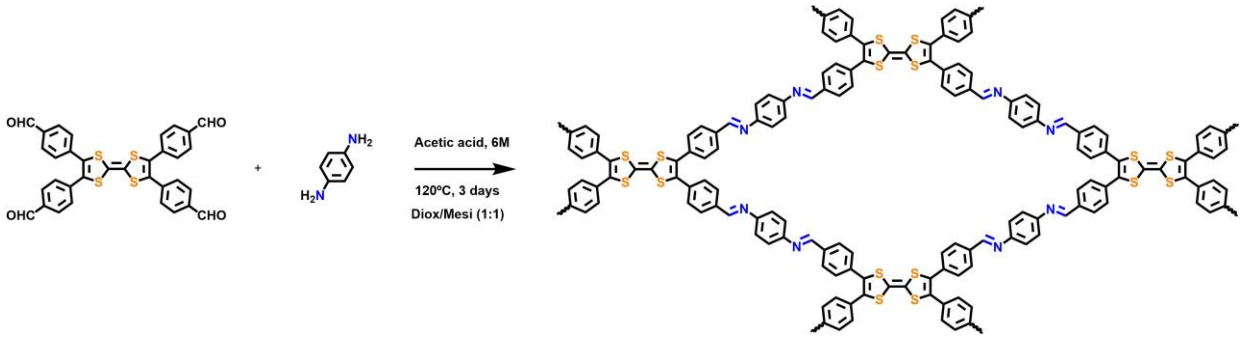

Scheme S1. Synthesis of TTF-Ph-COF.

TTF-Ph-COF was synthesized as previously described.[2–4] Tetrathiafulvalene tetrabenzaldehyde (TTF-TBA) (13.6 mg, 0.022 mmol) and phenylenediamine (4.8 mg, 0.044 mmol) were dissolved in a solution of mesitylene (0.5 mL), dioxane (0.5 mL) and aqueous acetic acid 6 M (0.1 mL) within a Pyrex glass tube (8 mL). The tube was heated at 120 ºC (heating rate of 1 ºC/min) for 3 days. Then, the reaction mixture was cooled to room temperature and the precipitate was washed with anhydrous THF to remove unreacted precursors and activated with supercritical CO_2 as described below obtaining 13.0 mg of **TTF-Ph-COF** (93 % yield). IR (cm^{-1}): 1695 (w), 1620 (m, C=N), 1600 (m), 1560 (w), 1507 (m), 1409 (m), 1307 (w), 1197 (m), 1169 (m), 1104 (w), 1014 (m), 826 (s), 781 (m), 721 (w).

2.2. Synthesis of TTF-(Ph)$_2$-COF

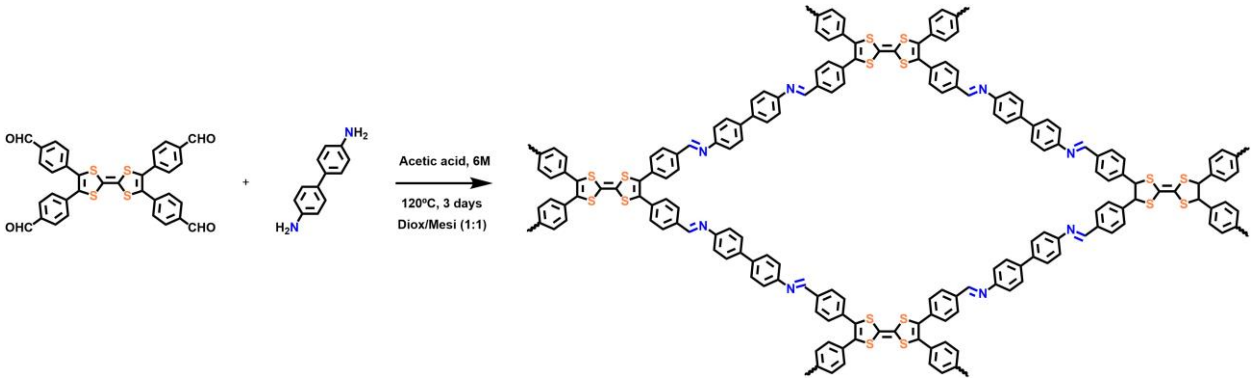

Scheme S2. Synthesis of TTF-(Ph)$_2$-COF.

Tetrathiafulvalene tetrabenzaldehyde (TTF-TBA) (12 mg, 0.019 mmol) and benzidine (7.5 mg, 0.041 mmol) were dissolved in a solution of mesitylene (1.0 mL), dioxane (1.0 mL) and aqueous acetic acid 6 M (0.2 mL) within a Pyrex glass tube (8 mL). The tube was heated at 120 ºC (heating rate of 1 ºC/min) for 3 days. Then, the reaction mixture was cooled to room temperature and the precipitate was washed with anhydrous THF to remove unreacted precursors and activated with supercritical CO_2 as described below obtaining 13.5 mg of **TTF-(Ph)$_2$-COF** (95 % yield). IR (cm^{-1}): 1693 (w), 1615 (m, C=N), 1598 (m), 1556 (m), 1524 (w), 1484 (m), 1408 (w), 1201 (w), 1167 (m), 815 (s), 783 (s).

2.3. Synthesis of TTF-BT-COF

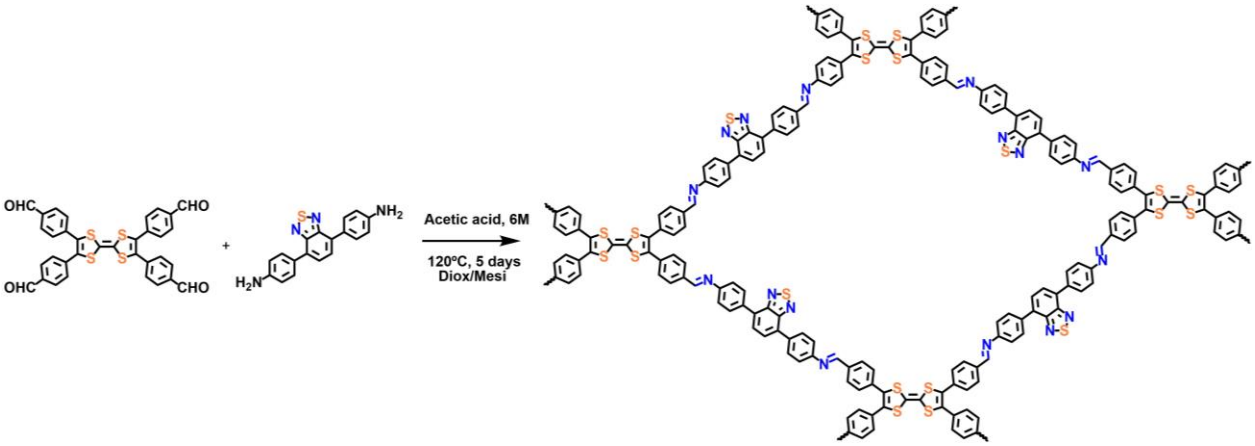

Scheme S3. Synthesis of **TTF-BT-COF**.

Tetrathiafulvalene tetrabenzaldehyde (TTF-TBA) (12.0 mg, 0.02 mmol) and 4,7-bis(4-aminophenyl)-2,1,3-benzothiadiazole (BT) (25.0 mg, 0.08 mmol) were mixed in dioxane (0.2 mL), mesitylene (1.8 mL) and 0.1 mL AcOH (6 M) within a Pyrex glass tube (8 mL). The mixture was sonicated for 10 minutes and then heated at 120 °C (heating rate of 1 ºC/min) for 5 days. Afterward, the reaction mixture was cooled to room temperature and the precipitate was activated with supercritical CO_2 as described below obtaining 17.0 mg of **TTF-BT-COF** (95 % yield). IR (cm^{-1}): 1693 (w), 1615 (m, C=N), 1595 (m), 1555 (m), 1515 (m), 1476 (s), 1407 (w), 1284 (w), 1202 (w), 1169 (m), 888 (s), 820 (s).

Covalent Organic Framework Activation

TTF-Ph-COF and **TTF-(Ph)$_2$-COF** samples were first washed with THF to remove unreacted monomers and then the solvent was exchanged with EtOH. Then, the samples, immersed in ethanol, were placed in dialysis tubing (Spectra/Por 1, MWCO: 6-8 kD). They were then introduced into an SPI-DRY Critical Point Dryer – Jumbo. The chamber was filled with liquid CO_2 at 10 ºC. After allowing it to exchange for 1 h, the reactor was flushed with fresh liquid CO_2. This solvent exchange procedure was performed a total of 5 times. Once the exchange process was completed, the temperature was raised to 40 ºC to exceed the critical point of CO_2. When the pressure stabilized around 90 bar, the chamber was slowly vented at a rate of 6 bar h^{-1} until atmospheric pressure was reached and the samples were recovered.

TTF-BT-COF was first washed with dioxane to remove residual monomers, then the solvent was exchanged with diethyl ether as an intermediate step and finally with perfluorohexane. Then, the samples, immersed in perfluorohexane, were placed in dialysis tubing. From this point on, the procedure was the same as above, the critical point dryer chamber was filled with liquid CO_2 and solvent exchange cycles were performed. Then, the temperature was raised, and once the supercritical conditions were achieved, the water was vented in a controlled fashion at 6 bar h^{-1}.

3. Physicochemical characterization of TTF-COFs

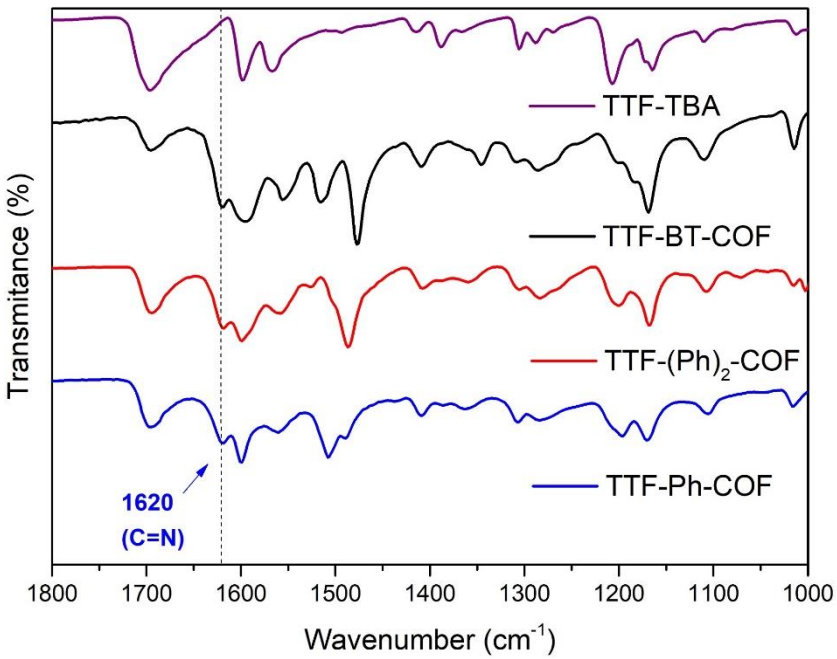

Figure S1. FT-IR spectra of TTF-TBA, TTF-Ph-COF, TTF-$(Ph)_2$-COF and TTF-BT-COF. The appearance of the new bands around 1620 cm^{-1} in TTF-COFs confirmed the formation of imine C=N linkage.

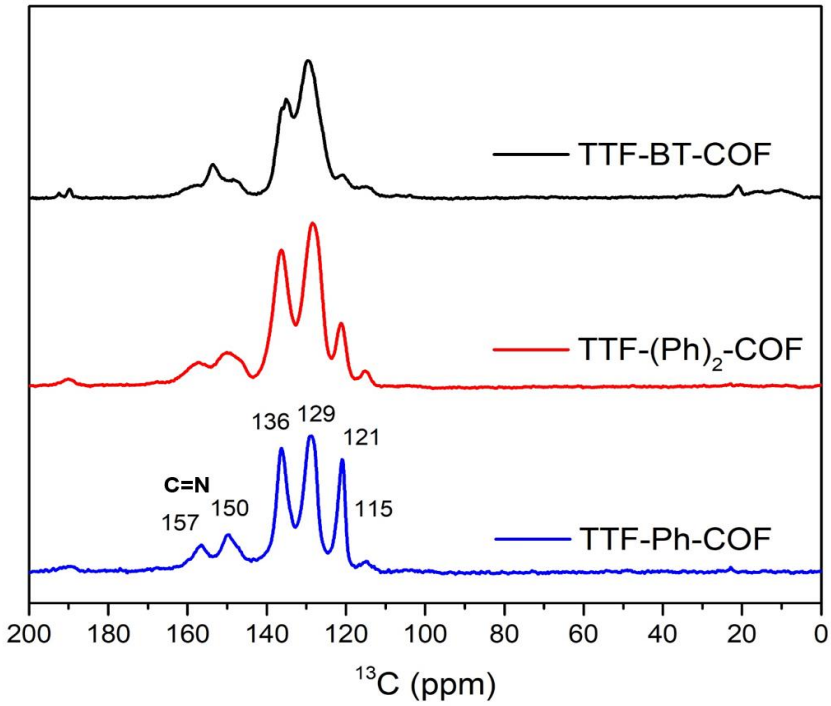

Figure S2. ^{13}C CPMAS NMR spectra of TTF-Ph-COF, TTF-$(Ph)_2$-COF and TTF-BT-COF at room temperature. The signals around 153-157 ppm are attributed to the formation of the C=N bond. The weak signals at 190 ppm are related to residual aldehyde groups.

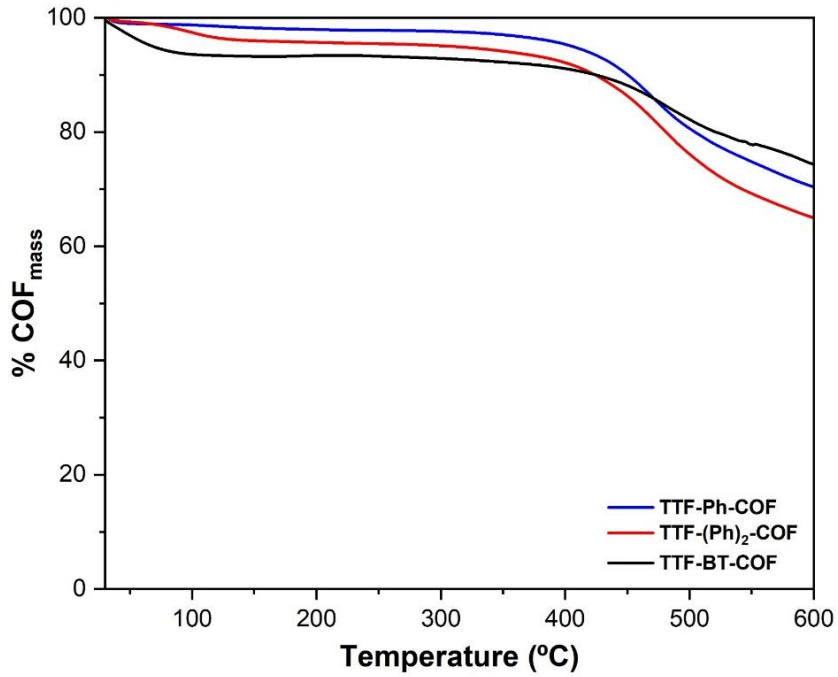

Figure S3. TGA profile recorded for TTF-Ph-COF, TTF-$(Ph)_2$-COF and TTF-BT-COF at a heating rate of 5 ºC min^{-1} under a constant stream of N_2.

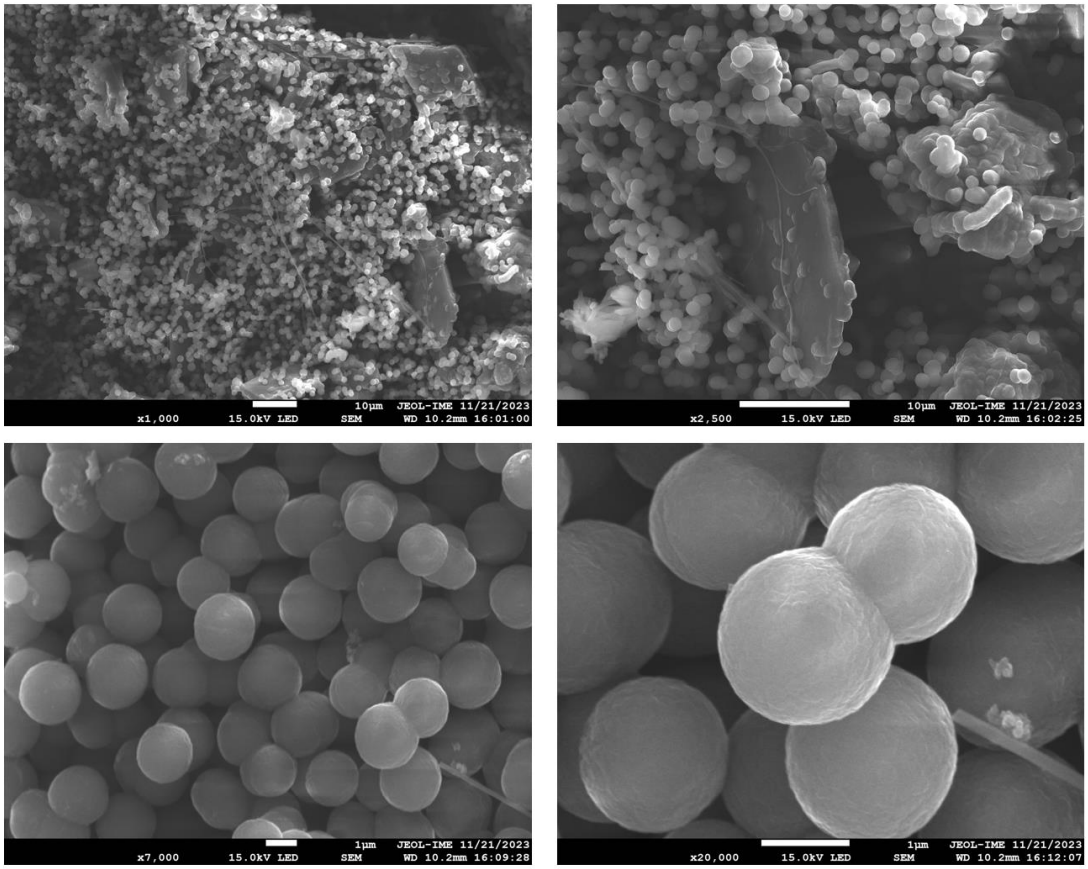

Figure S4. SEM images of TTF-Ph-COF.

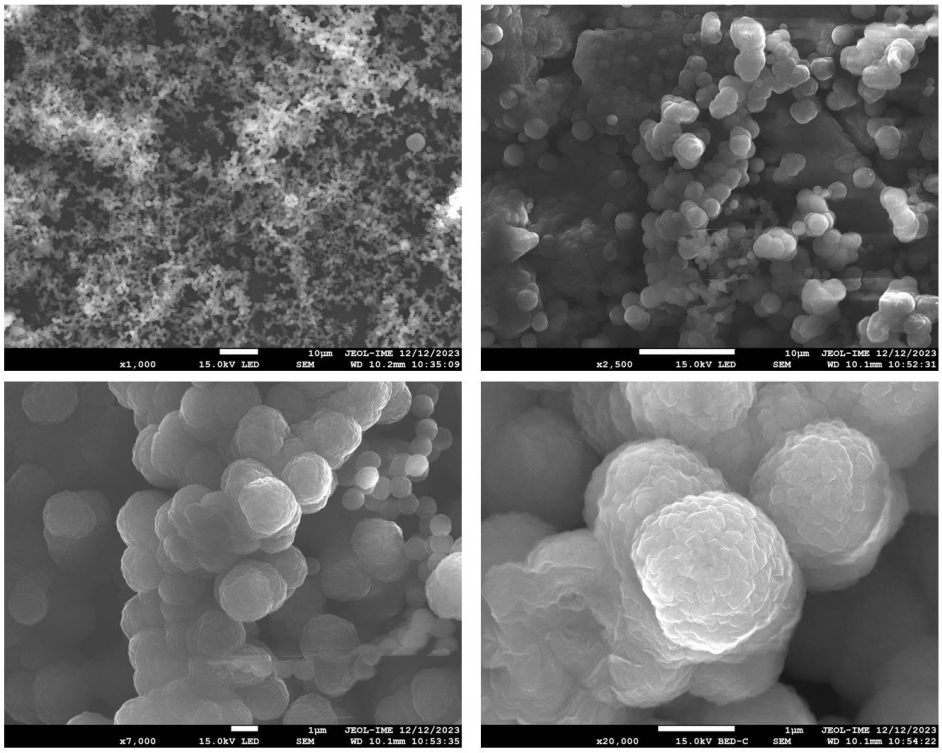

Figure S5. SEM images of TTF-$(Ph)_2$-COF.

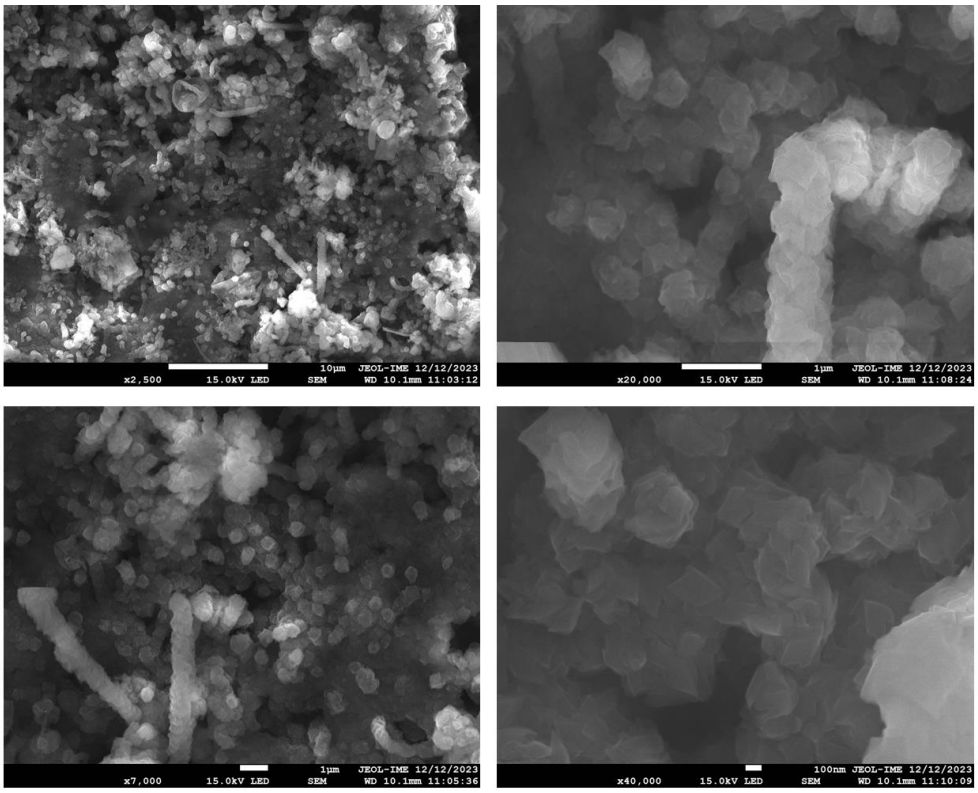

Figure S6. SEM images of TTF-BT-COF.

4. Computational modelling

Tight Binding (TB) calculations were systematically used to screen and preoptimize possible conformations and stackings prior DFT calculations. For this, the 3OB parameter set with D4 dispersion corrections was used[5–7] as implemented in the DFTB+ package.[8] Then, geometry optimizations on selected structures were performed with DFT with the PBE[9,10] functional augmented with Many Body Dispersion corrections[11,12] with the FHI-AIMS[13–15] program with "light_194" and "light" numerical orbitals, using the frozen core approximation with a -200 eV cutoff value. The band structure and corresponding gaps were computed with a B3LYP hybrid functional,[16–19] and porosities were computed with Poreblazer 4.0.[20,21]

Spanning from the inherent molecular flexibility of the linkers, several possible conformers of monolayer systems were investigated. Trial monolayers were built by hand, from the conformations obtained from the CREST software,[22] and from MD simulations and optimized at the PBE+MBD/light level, see Table S1 and Figure S6. The differences in energy between the computed monolayer conformers for each COF were found to be often negligible, which suggests that various conformers may be present concurrently in extended monolayers.

Table S1. Selected explored monolayers of TTF-COFs.

system	geometry	Energy	Energy difference	a	b	c
		eV	meV	Å	Å	Å
TTF-Ph-COF	MD	-97397.5569	0	28.90	29.02	100.00
	CREST	-97397.551	6	28.76	28.96	100.00
	by hand	-97397.5352	22	28.91	29.02	100.00
TTF-$(Ph)_2$-COF	MD	-109961.3657	0	24.68	24.71	100.00
	by hand	-109961.3655	0	24.49	24.80	100.00
	CREST	-109961.3241	42	24.37	24.67	100.00
TTF-BT-COF	MD	-150079.0351	0	33.15	33.46	100.00
	CREST	-150079.0303	5	33.18	33.40	100.00
	by hand	-150078.9986	37	33.43	33.42	100.00

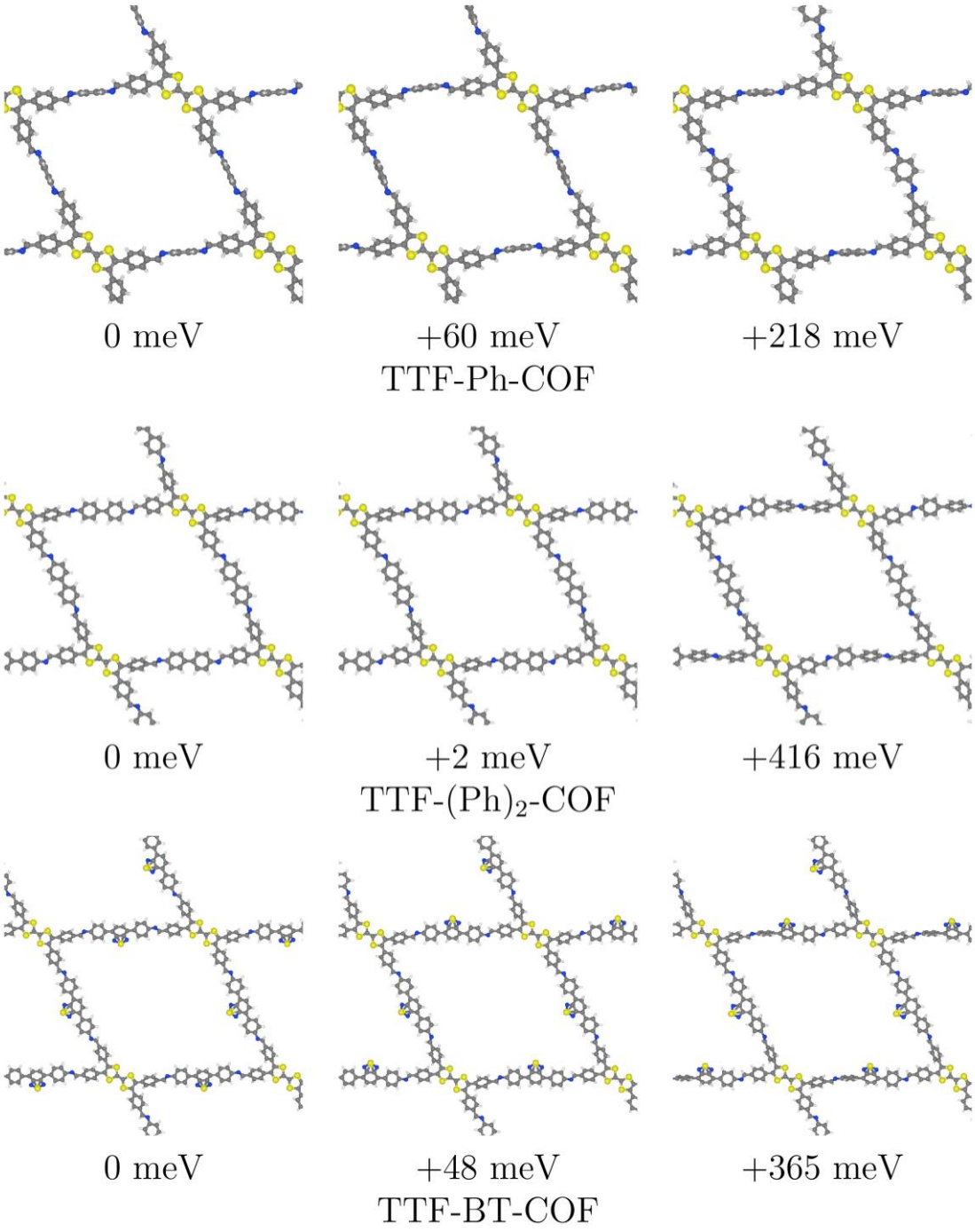

Figure S7. Monolayer of TTF-COFs and their relative energies.

The relative binding energy, defined as $BE = E_{bulk} - 2 \cdot E_{monolayer}$, was chosen as a comparative measure of thermodynamic stability of bulk systems made by two monolayers. Several possible initial bulk structures were tried, including different layer stackings, arrangements of imine bonds, and BT orientation arrangements (for **TTF-BT-COF**). All structures were first optimized using Tight Binding, and later using DFT (PBE-MBD@rsSCS/light Hamiltonian, with Γ-centered 3x3x2 k-point grid), until the maximum force per atom was smaller than 0.05 eV/Å. Table S2 summarizes the so-obtained structures. It was found that the AA stacking showed systematically lower energies, compared to AB stacking. Furthermore, as expected from their structure, AB stackings showed consistently thinner pores, see Table S4 and Figures S8-S10, compared to AA with matched better experimental measurements. Furthermore, the simulated XRD pattern of the computed AB stacked bulk COFs structures, showed peaks at higher 2θ angles which were not present in the experimental spectra, see Table S3 and Figures S11-S13.

Table S2. Investigated bulk TTF-COFs with different conformations and stackings.

system	Stacking	Conformation	Energy	Energy difference	Binding energy	Binding energy per atom
			eV	meV	eV	meV
TTF-Ph-COF	AA	v1	-194798.752	0	-3.64	-22
	AA	v2	-194798.603	149	-3.49	-21
	AA	v3	-194798.599	153	-3.49	-21
	AA	v4	-194798.597	155	-3.48	-21
	AA	v5	-194798.593	159	-3.48	-21
	AA	v6	-194798.584	168	-3.47	-21
	AA	v7	-194798.489	264	-3.37	-21
	AA	v8	-194798.434	318	-3.32	-20
	AA	v9	-194798.331	421	-3.22	-20
	AA	v10	-194798.226	526	-3.11	-19
	AA	v11	-194798.226	527	-3.11	-19
	AA	v12	-194798.219	534	-3.10	-19
	AA	v13	-194797.930	822	-2.82	-17
	AB	v1	-194796.181	2572	-1.07	-7
TTF-$(Ph)_2$-COF	AA	v1	-219927.143	0	-4.41	-22

	AA	v2	-219926.807	336	-4.08	-20
	AA	v3	-219926.806	338	-4.07	-20
	AA	v4	-219926.798	345	-4.07	-20
	AA	v5	-219926.776	368	-4.04	-20
	AB	v1	-219925.029	2114	-2.30	-11
TTF-BTD-COF	AA	v1	-300163.636	0	-5.57	-22
	AA	v2	-300163.596	40	-5.53	-22
	AA	v3	-300163.542	94	-5.47	-22
	AA	v4 anti BT	-300163.521	115	-5.45	-22
	AA	v5	-300163.496	140	-5.43	-22
	AA	v6 anti BT	-300163.492	144	-5.42	-22
	AA	v7 anti BT	-300163.488	148	-5.42	-22
	AA	v8	-300163.487	149	-5.42	-22
	AA	v9 anti BT	-300163.429	207	-5.36	-22
	AA	v10	-300163.377	259	-5.31	-21
	AA	v11 anti BT	-300162.966	670	-4.90	-20
	AB	v1	-300162.222	1414	-4.15	-17
	AB	v2	-300160.869	2767	-2.80	-11
	AB	v3	-300160.659	2977	-2.59	-10

Table S3. Unit cells of TTF-based COFs for structures optimized at PBE-MBD/light_194 level.

System	**Stacking**	**Density**	**a**	**b**	**c**	**alpha**	**beta**	**gamma**
		g/cm³	Å	Å	Å	°	°	°
TTF-Ph-COF	AA	0.62	24.27	24.30	7.36	90	89	110
	AB	0.54	24.32	24.69	8.97	90	90	119
	ML		24.37	24.67	100.0	90	90	120
TTF-$(Ph)_2$-COF	AA	0.54	28.55	28.69	7.39	90	89	110
	AB	0.63	28.81	28.96	6.47	86	90	117
	ML	0.02	28.91	29.02	100.0	90	90	120
TTF-BT-COF	AA	0.50	32.93	33.10	7.83	101	76	104
	AB	0.81	32.40	33.10	7.55	91	39	104
	ML		33.43	33.42	100.00	90	90	120

Table S4. Porosities of the modelled TTF-COFs

System	Stacking	Pore Limiting Diameter	Pore accessible Surface Area	Pore accessible Volume
		Å	m^2/g	cm^3/g
TTF-Ph-COF	AA	14.92	1769	0.932
	AB	9.40	3458	1.211
TTF-$(Ph)_2$-COF	AA	18.24	2175	1.174
	AB	10.27	1924	0.841
TTF-BT-COF	AA	21.18	2177	1.345
	AB	7.98	3215	0.468

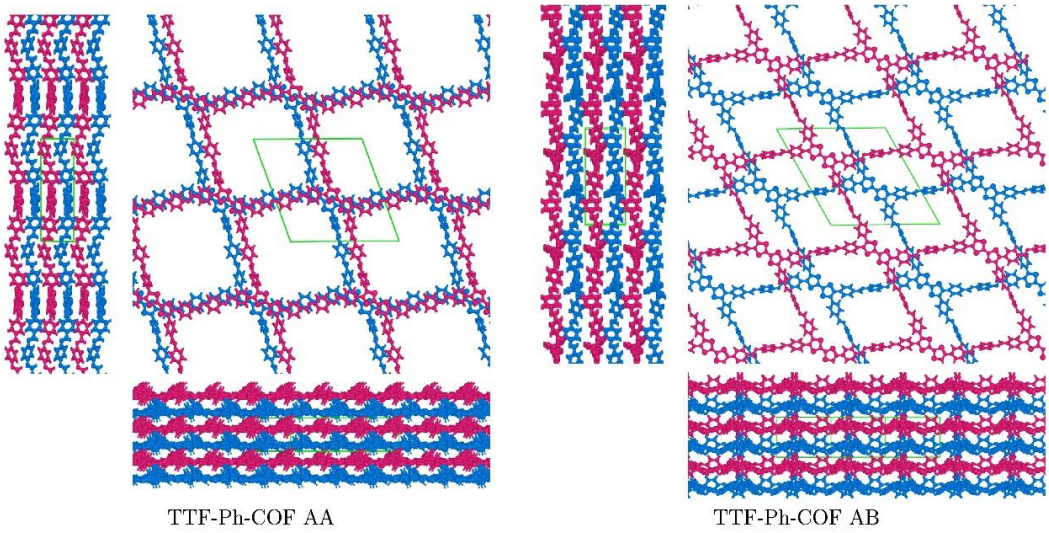

Figure S8. AA and AB modelled bulk structures of TTF-Ph-COF.

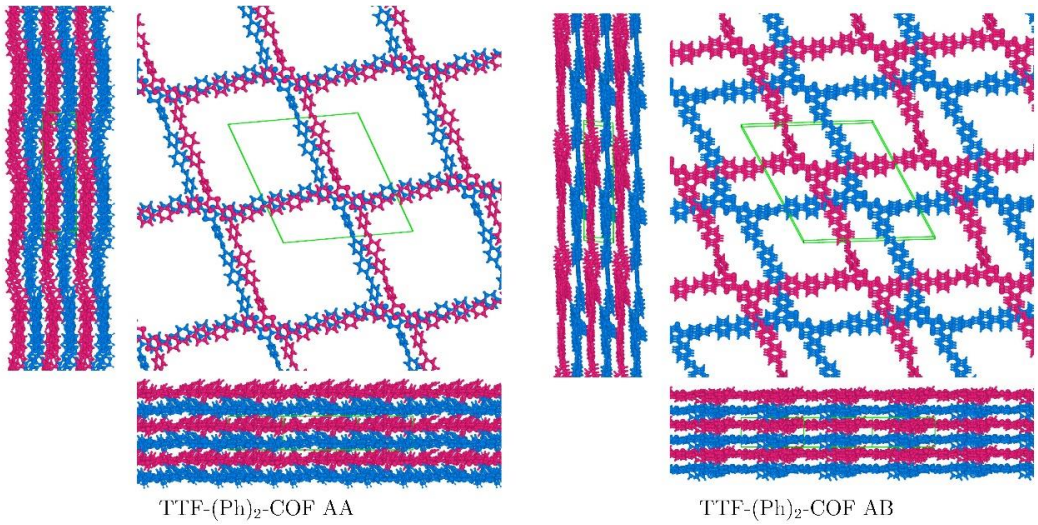

Figure S9. AA and AB modelled bulk structures of TTF-$(Ph)_2$-COF.

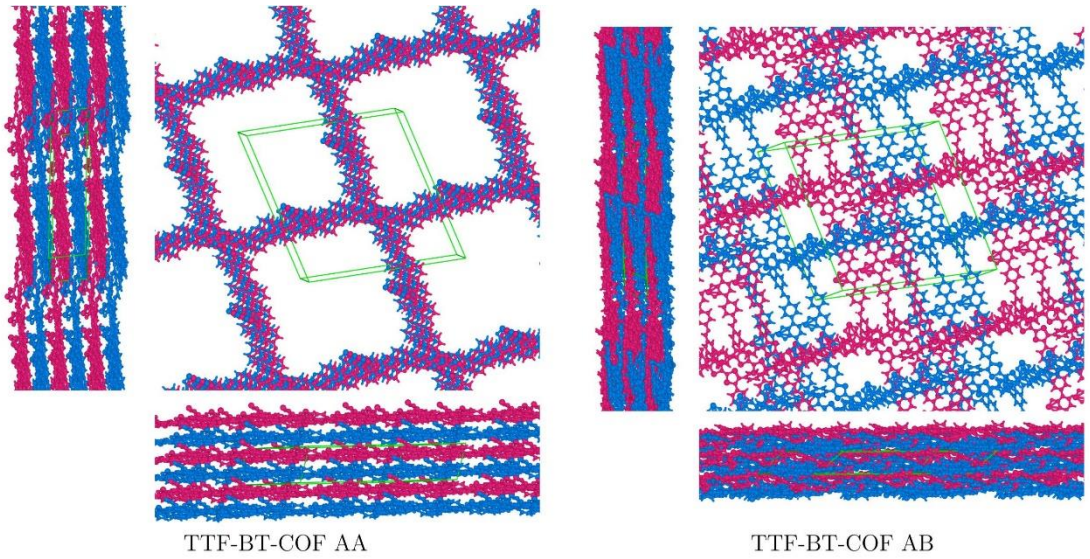

Figure S10. AA and AB modelled bulk structures of TTF-BT-COF.

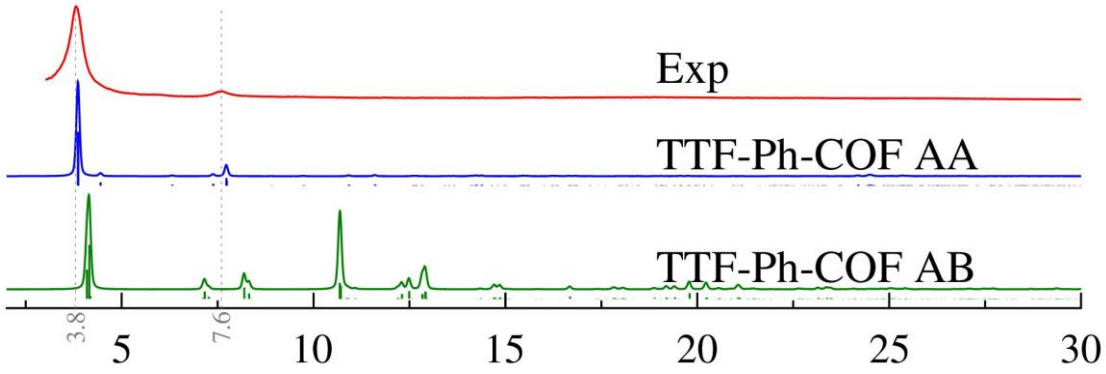

Figure S11. Simulated versus experimental PXRD for TTF-Ph-COF.

.

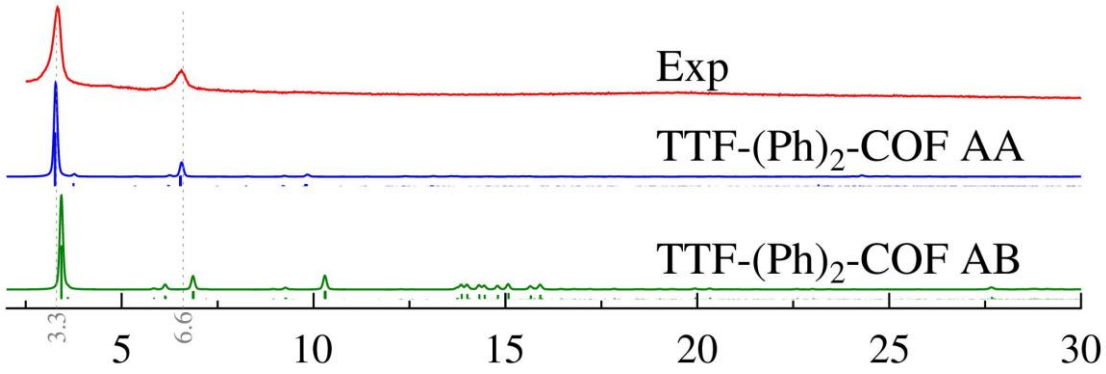

Figure S12. Simulated versus experimental PXRD for TTF-$(Ph)_2$-COF.

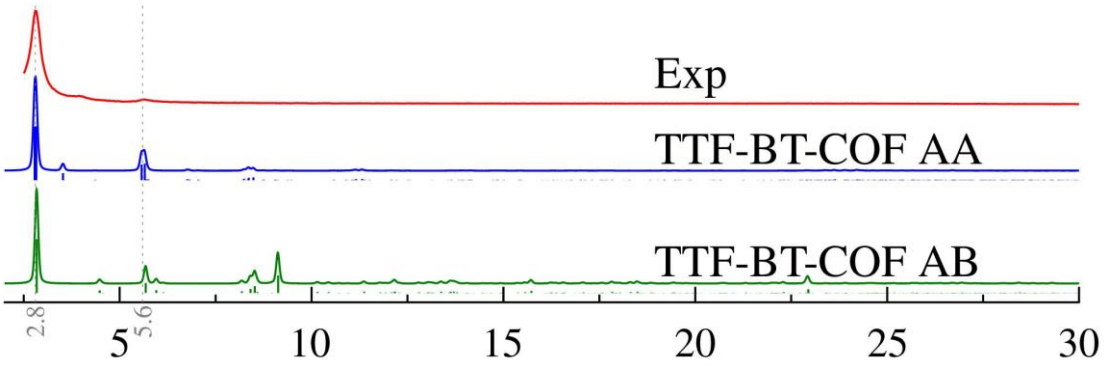

Figure S13. Simulated versus experimental PXRD for TTF-BT-COF.

5. Porosity Measurements

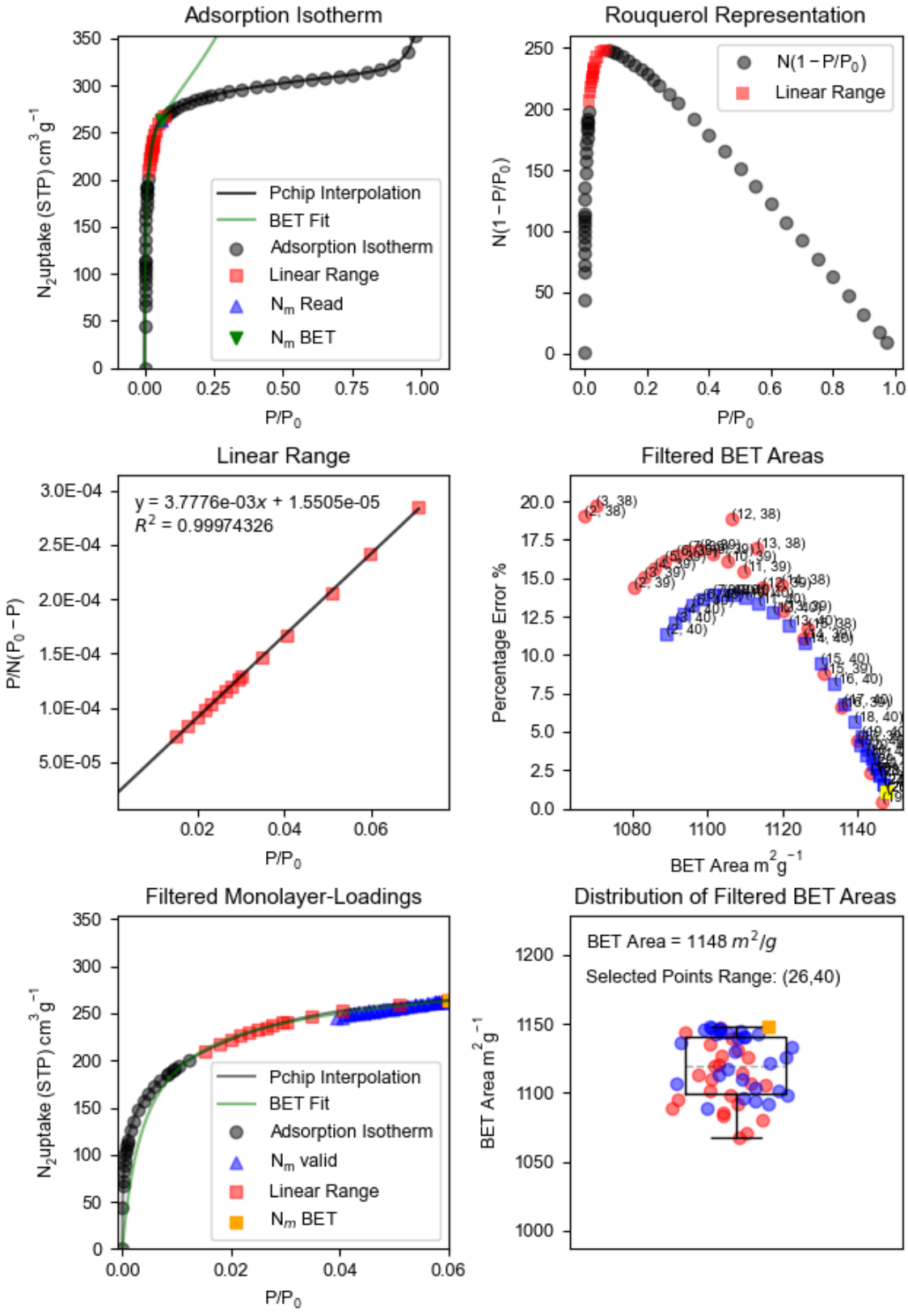

Figure S14. BETSI regression diagnostics for TTF-Ph-COF.

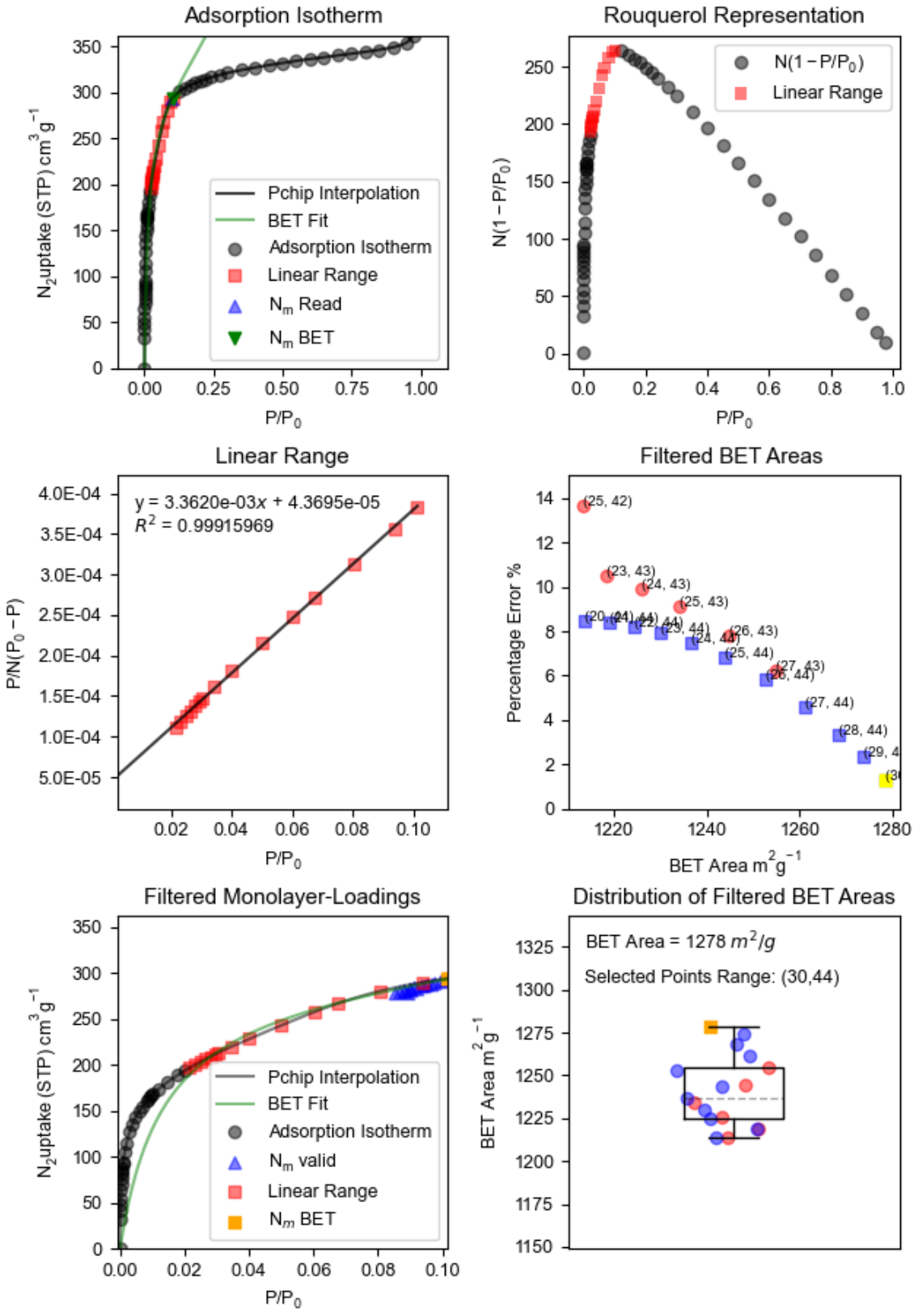

Figure S15. BETSI regression diagnostics for TTF-$(Ph)_2$-COF.

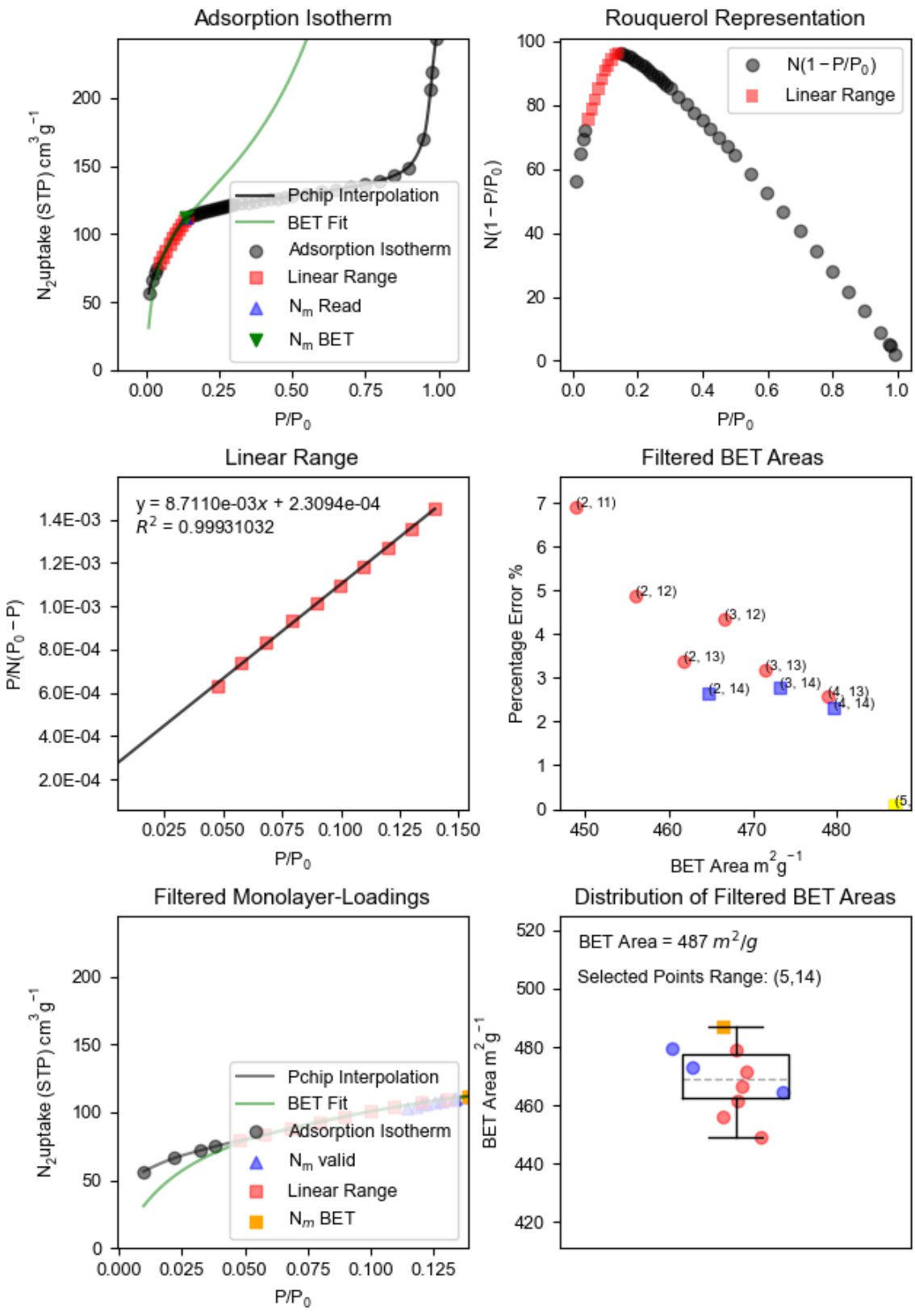

Figure S16. BETSI regression diagnostics for TTF-BT-COF.

6. Chemical doping of TTF-COFs

Doping with iodine: A 20 mL vial was charged with 30 g of iodine. A small vial (4 mL) filled with the COFs was left in the 20 mL vial, which was further capped tightly and kept in the dark at room temperature for 48h.

Doping with F_4TCNQ: The COFs bulk powders were stirred in the acetonitrile/F_4TCNQ solution for one hour. The concentration of the solution was calculated to have 1 eq. of F_4TCNQ compared to the number of electroactive species.

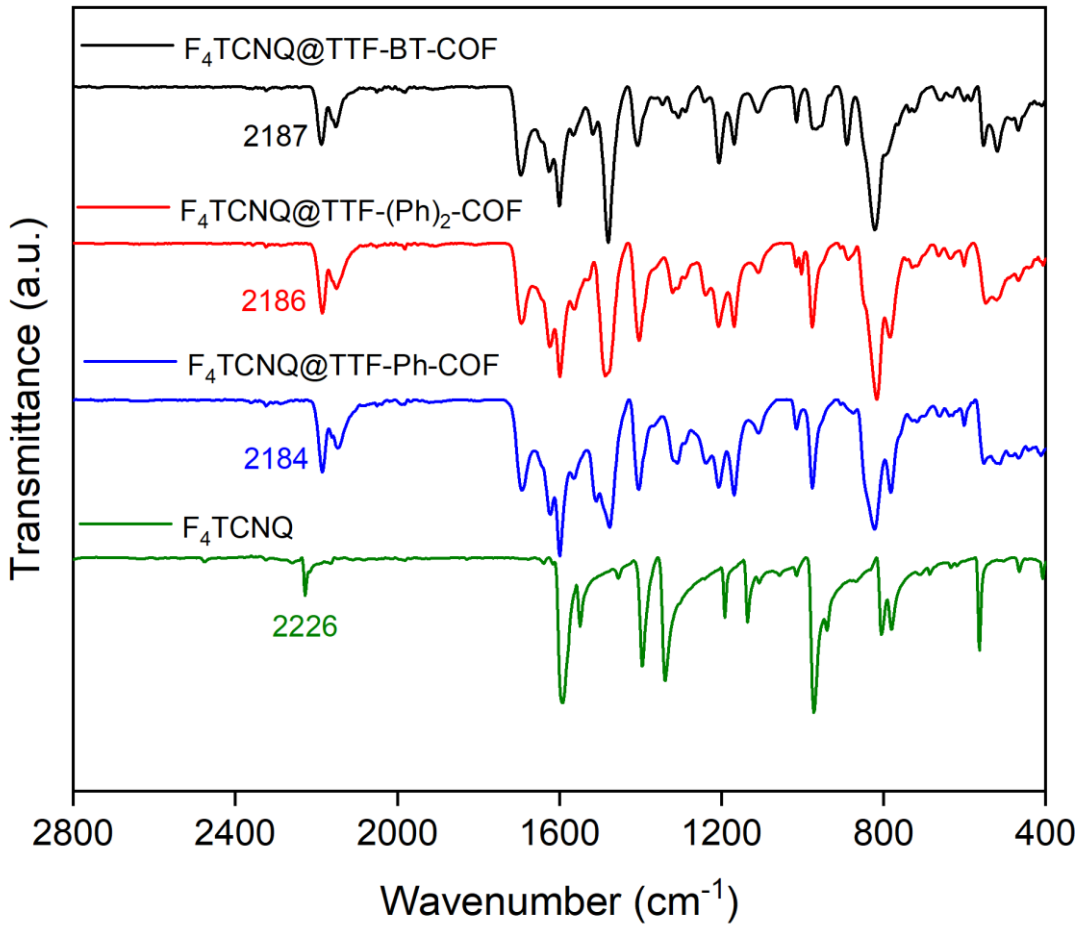

Figure S17. IR spectra of F_4TCNQ, TTF-Ph-COF/F_4TCNQ, TTF-$(Ph)_2$-COF/F_4TCNQ and TTF-BT-COF/F_4TCNQ.

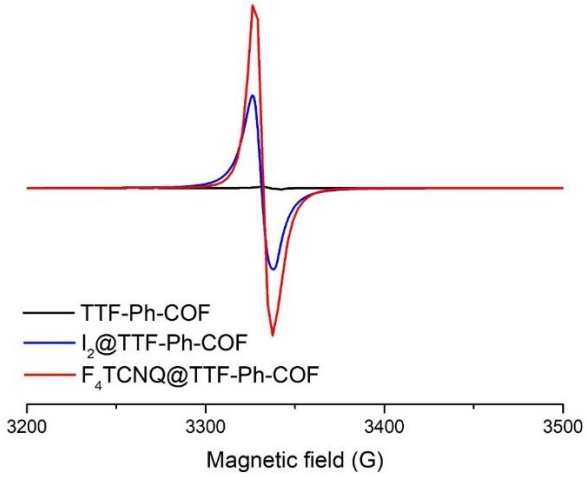

Figure S18. EPR spectra of TTF-Ph-COF, TTF-Ph-COF/iodine and TTF-Ph-COF/F_4TCNQ (1 eq.) at room temperature.

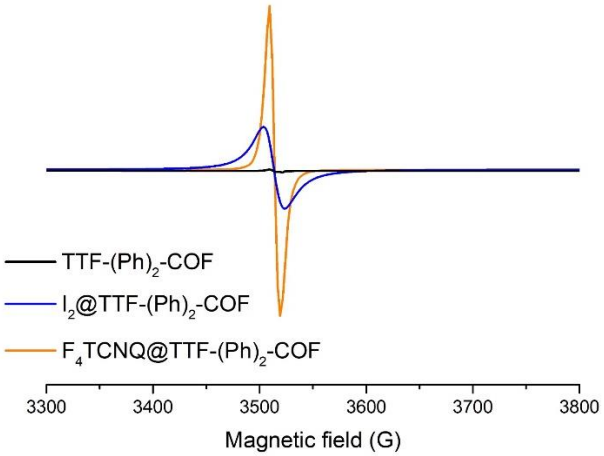

Figure S19. EPR spectra of TTF-$(Ph)_2$-COF, TTF-$(Ph)_2$-COF/I_2 and TTF-$(Ph)_2$-COF/F_4TCNQ (1 eq.) at room temperature.

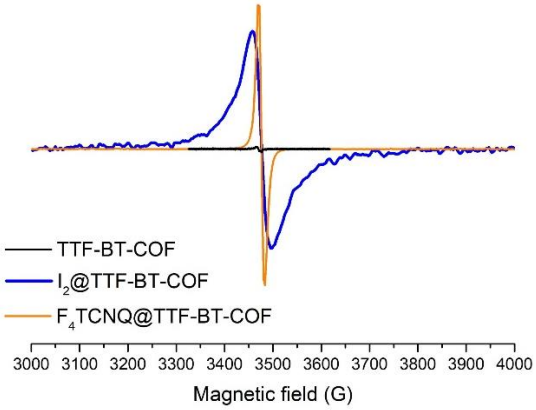

Figure S20. EPR spectra of TTF-BT-COF, TTF-BT-COF/I_2 and TTF-BT-COF/F_4TCNQ (1 eq.) at room temperature.

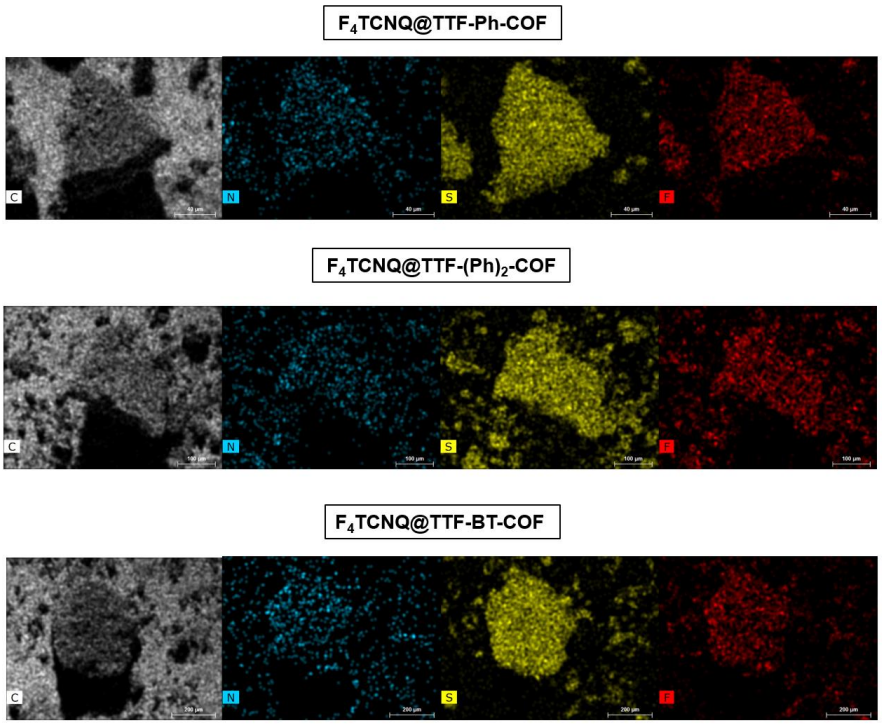

Figure S21. SEM images and energy dispersive X-ray spectroscopy for F_4TCNQ-doped TTF-COFs.

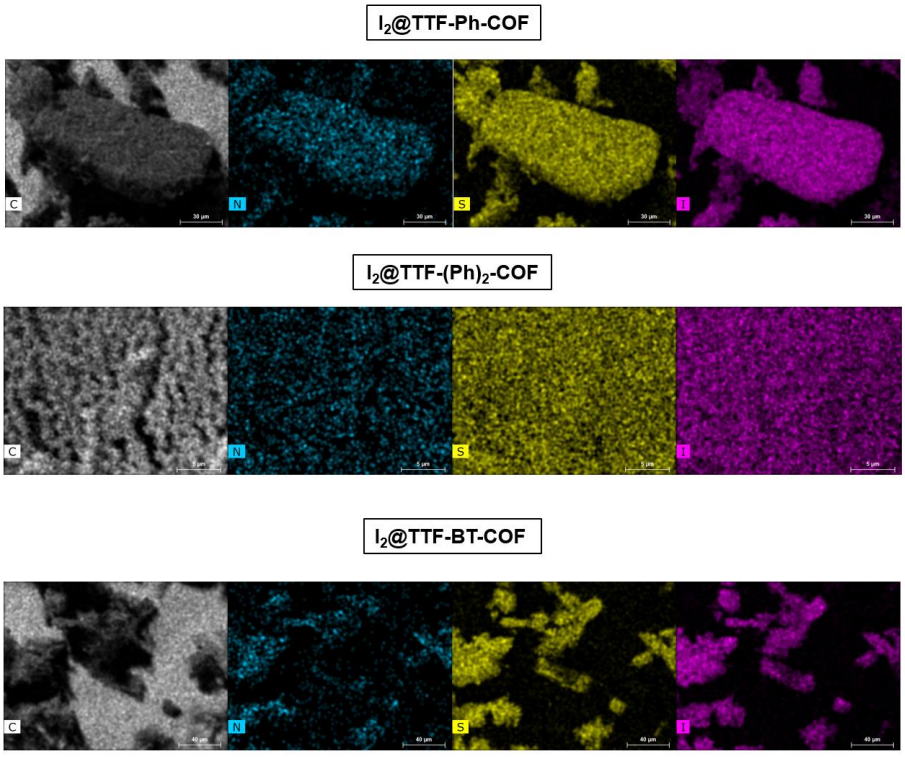

Figure S22. SEM images and energy dispersive X-ray spectroscopy for iodine-doped TTF-COFs.

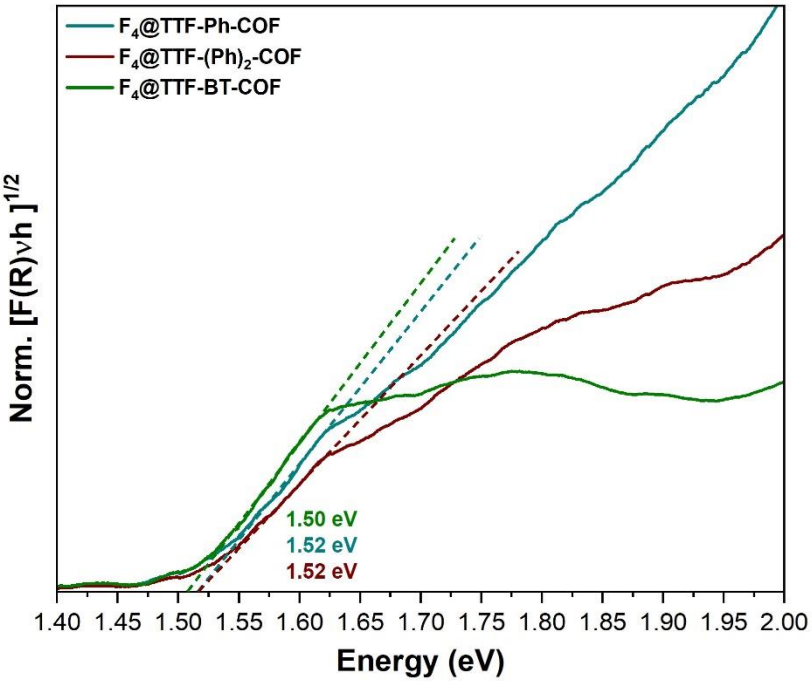

Figure S23. Normalized Tauc plot of the Kubelka–Munk-transformed data for TTF-Ph-COF/F_4TCNQ, TTF-$(Ph)_2$-COF/F_4TCNQ and TTF-BT-COF/F_4TCNQ. Dashed lines indicate linear fits to the absorption onsets.

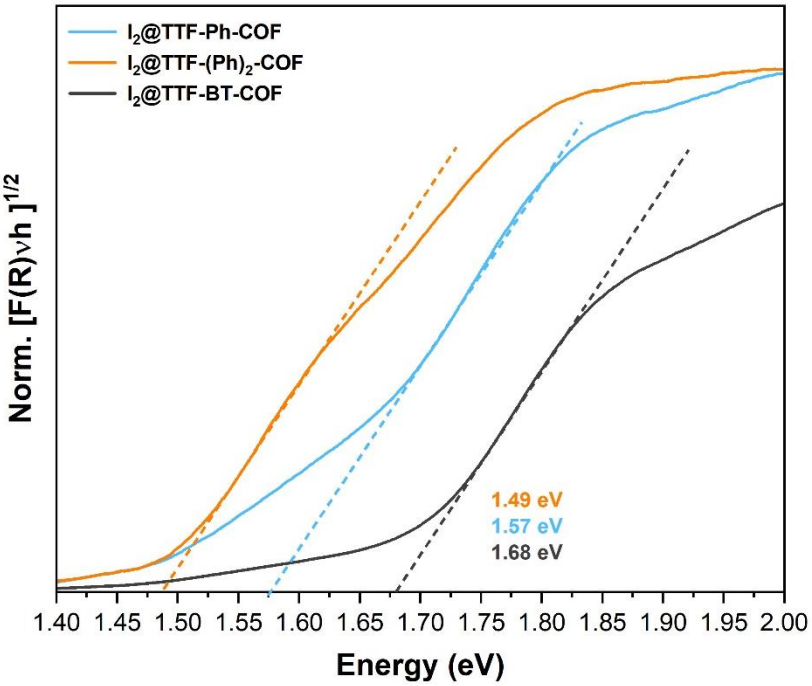

Figure S24. Normalized Tauc plot of the Kubelka–Munk-transformed data for TTF-Ph-COF/I_2, TTF-$(Ph)_2$-COF/I_2 and TTF-BT-COF/I_2. Dashed lines indicate linear fits to the absorption onsets.

Theoretical calculations using the B3LYP hybrid functional were carried out to study the electronic structure of TTF-COFs for the ML system with a 3x3x1 k-point grid with the light_194 basis set, Table S5. Figure S25 shows the band structures for **TTF-Ph-COF** and **TTF-(Ph)$_2$-COF**. Figures S26 and S27 show the integrated electron density of frontier orbitals of **TTF-Ph-COF** and **TTF-(Ph)$_2$-COF**, respectively. Figure S28 illustrates the frontier orbitals eigenvalues of iodine and F_4TCNQ frontier orbitals with respect to the bands of TTF COF monolayers.

Table S5. Band gaps and frontier HOCO and LUCO maximum and minimum energies respectively for monolayer TTF COFs.

System	HOCO	HOCO vs. Ag	LUCO	LUCO vs. Ag	Band gap
	eV	V	eV	V	eV
TTF-Ph-COF	-4.93	0.47	-2.87	-1.59	2.07
TTF-(Ph)$_2$-COF	-4.99	0.53	-2.84	-1.62	2.15
TTF-BT-COF	-4.98	0.52	-3.04	-1.42	1.94

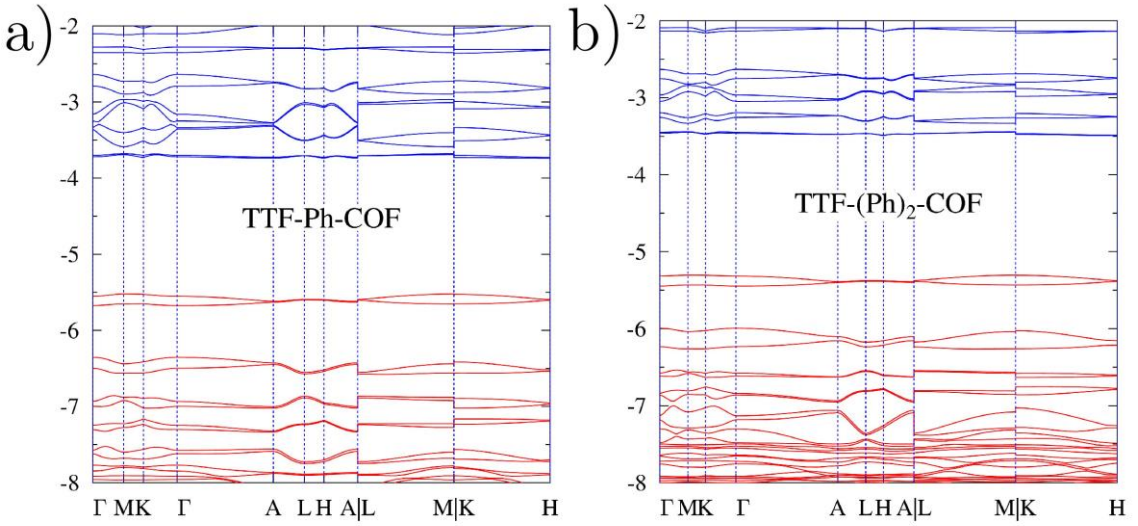

Figure S25. Computed band structures of a) TTF-Ph-COF and b) TTF-(Ph)$_2$-COF using B3LYP functional. Red and blue lines indicate occupied and unoccupied levels, respectively.

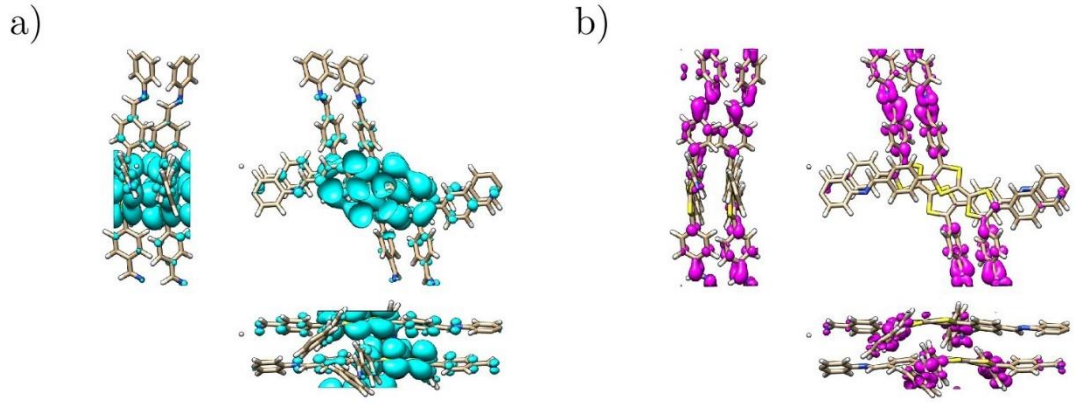

Figure S26. Integrated electronic density for TTF-Ph-COF for the two highest occupied bands (a) and the two lowest unoccupied bands (b).

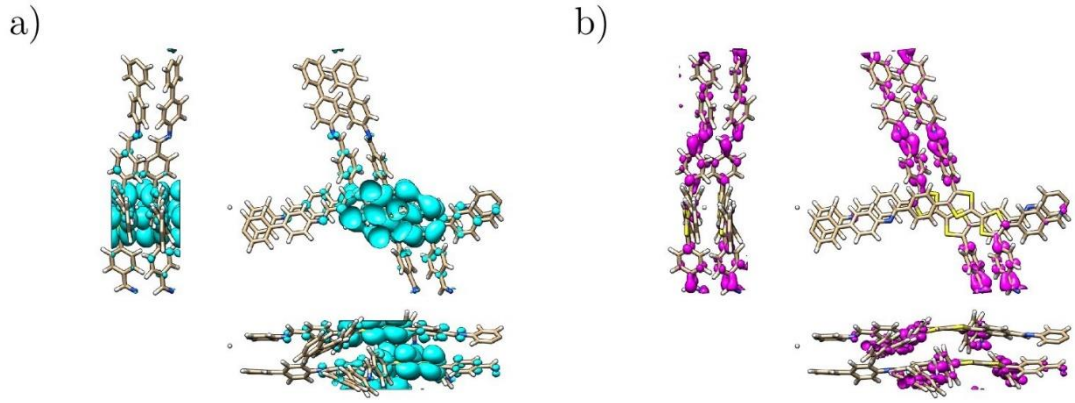

Figure S27. Integrated electronic density for TTF-$(Ph)_2$-COF for the two highest occupied bands (a) and the two lowest unoccupied bands (b).

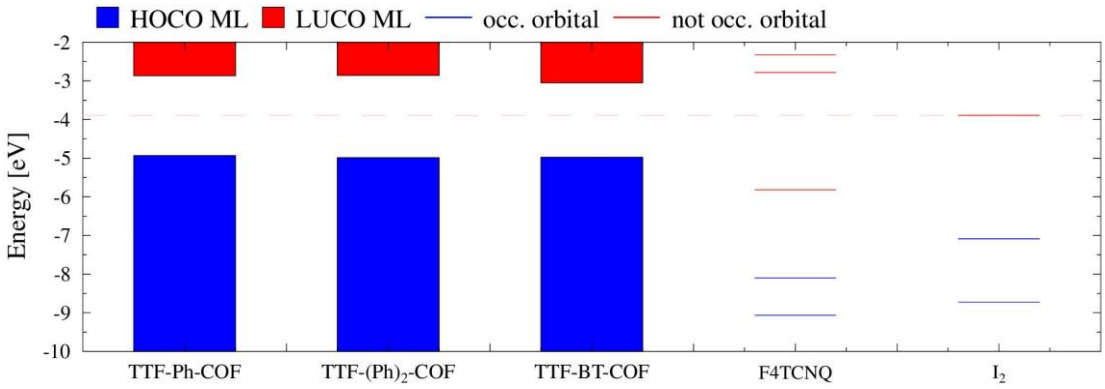

Figure S28. Occupied and unoccupied bands maximum and minimum energies for monolayer TTF-COFs and molecular orbitals eigenvalues of F_4TCNQ and I_2 computed with a B3LYP/light_194 Hamiltonian.

7. Electrochemical characterization of TTF-COFs

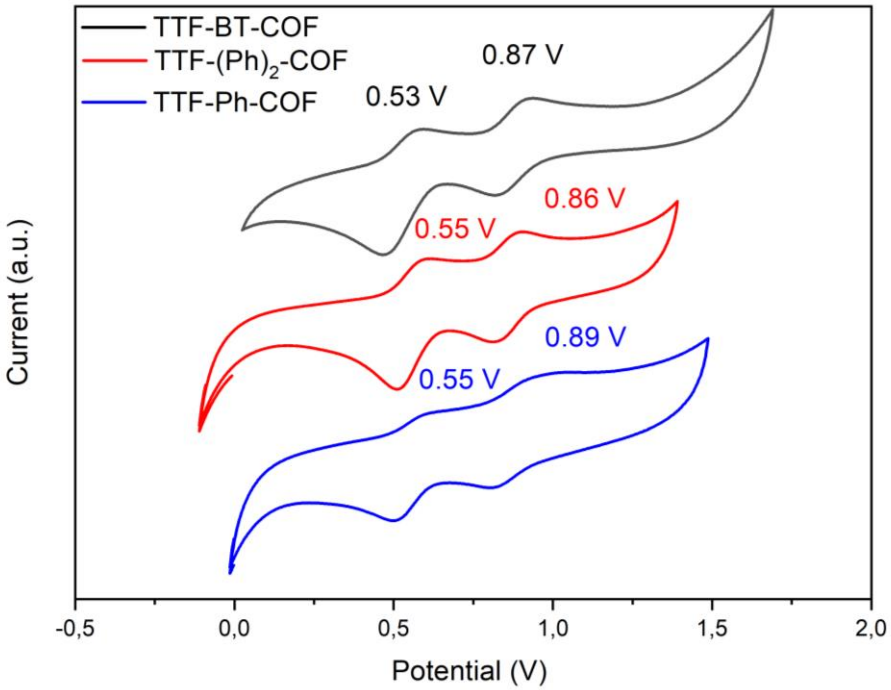

Figure S29. Solid-state cyclic voltammetry of **TTF-Ph-COF**, **TTF-(Ph)$_2$-COF**, and **TTF-BT-COF** in 0.1 M $TBAPF_6$ /CH_3CN as the electrolyte at 0.1 V s^{-1}. All potentials are quoted versus Ag_{wire}.

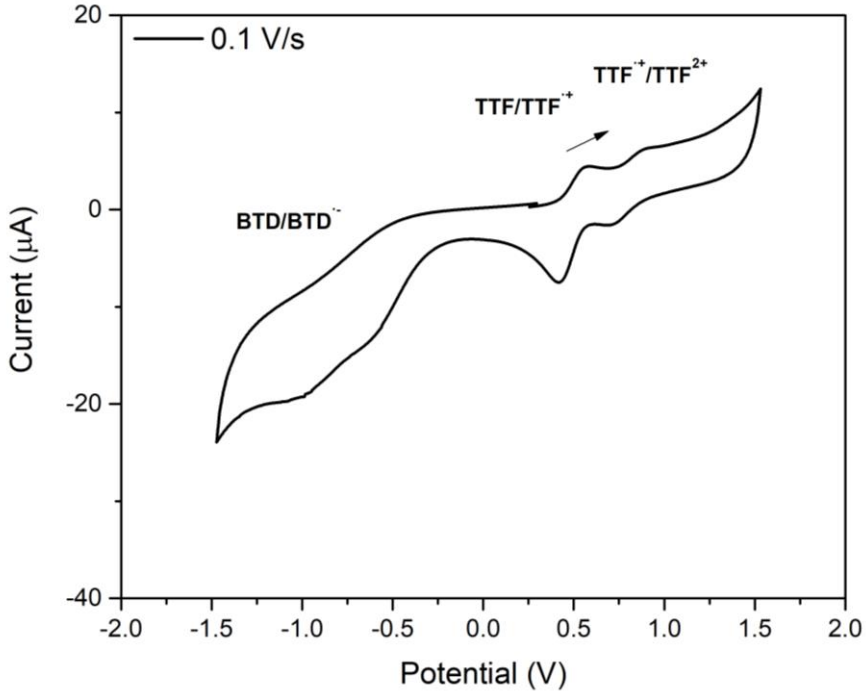

Figure S30. Solid-state cyclic voltammetry of **TTF-BT-COF** in 0.1 M $TBAPF_6$ /CH_3CN as the electrolyte at 0.1 V s^{-1} in the -1.5 – 2 V range. All potentials are quoted versus Ag_{wire}.

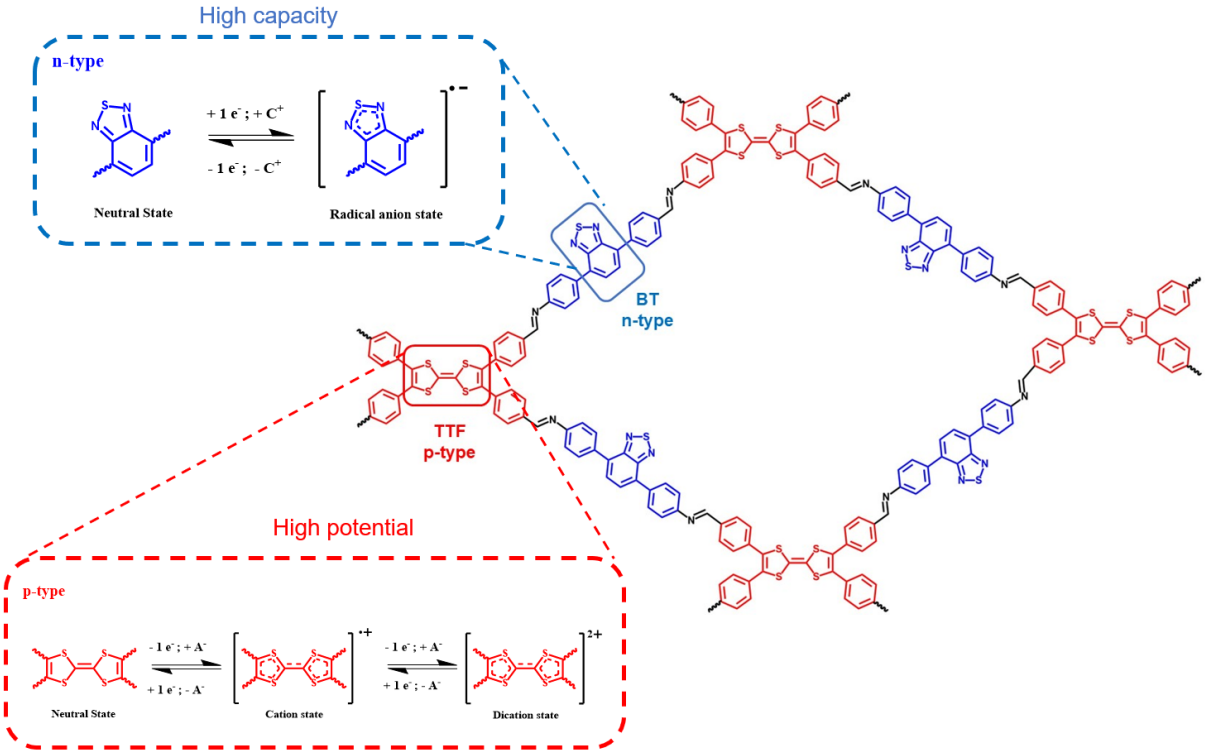

Figure S31. Redox processes of p-type TTF and n-type BT building blocks. C^+ stands for monovalent cation and A^- stands for monovalent anion.

Buckypaper Preparation

The process of preparing the buckypapers involved several steps. The electrode composition targeted was 50/35/15 of COF, single-walled carbon nanotubes (SWCNTs) and reduced graphene oxide (rGO), respectively. First, the single-walled carbon nanotubes (SWCNTs) were weighed and dispersed in N-Methyl-2-pyrrolidone (NMP), followed by 15 minutes of tip sonication to ensure even distribution. Next, rGO and COF were weighed and ground in a mortar and pestle and then added to the SWCNTs dispersion in NMP. This mixture underwent 5 minutes of tip sonication and an hour of bath sonication. Afterward, the mixture was left to stir overnight. Following stirring, an additional hour of bath sonication was carried out, followed by vacuum filtration using a Nylon membrane filter (45 mm). The buckypaper was first left to dry under vacuum at room temperature, followed by overnight drying at 80 °C also under vacuum conditions. The electrodes were fabricated with a target mass loading of active-material (TTF-COFs) of 1 mg cm^{-2}. As a commonly used procedure for organic batteries, specific capacities were calculated based on the amount of the active material.

Li-ion half-cell fabrication

The previously prepared buckypaper electrodes were cut into circular discs with 6 mm of diameter, weighted, and moved to an Ar-filled glovebox to be used in the cell assembly. Half-cells were assembled using a CR2032 coin-cell set-up with the self-standing buckypaper COF as the positive electrode. Lithium metal foil, with a 10 mm diameter, was used as the reference and counter electrode with a Whatmann (GF/A) glass fiber separator soaked with the liquid electrolyte (100 µl), 1 M lithium hexafluorophosphate ($LiPF_6$) in a mixture of ethylene carbonate (EC) and dimethyl carbonate (DMC), EC/DMC (3/7 v/v).

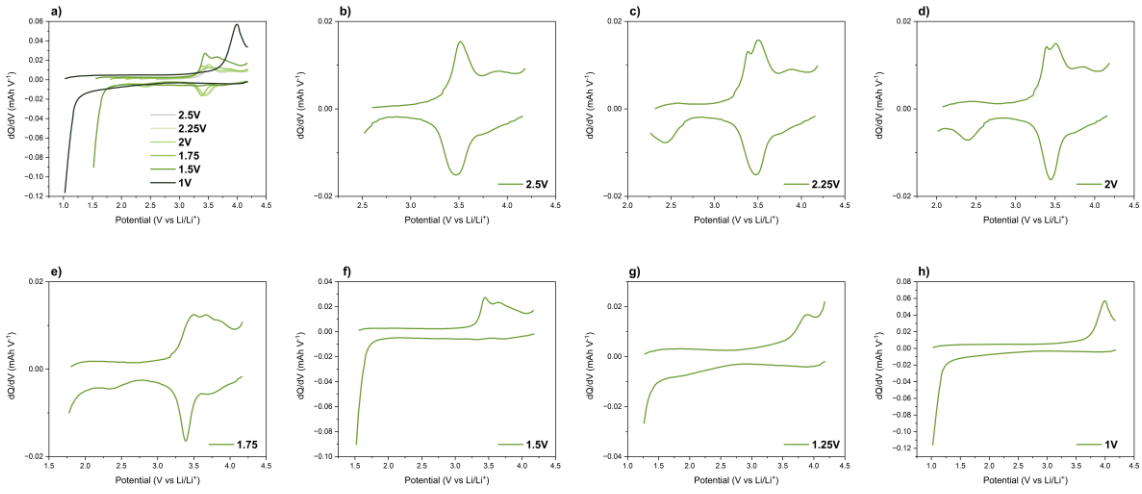

Figure S32. Differential capacity (dQ/dV) plots recorded at 5C for **TTF-BT-COF**, fixing potential upper cut-off limit at 4.2 V, while stepwise decreasing the lower cut-off limit to 1 V.

Cyclic Voltammetry

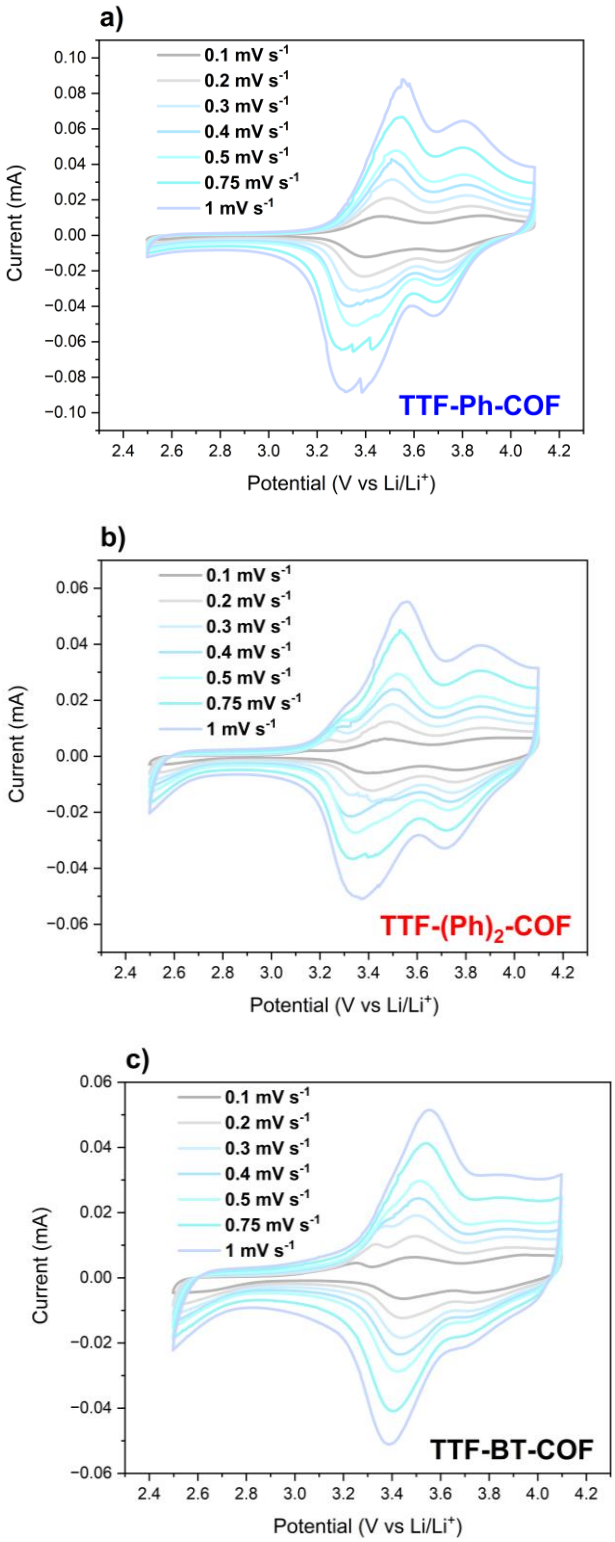

Figure S33. Cyclic Voltammetry of **TTF-Ph-COF**, **TTF-(Ph)$_2$-COF** and **TTF-BT-COF** at various scan rates ranging from 0.1 mV s^{-1} up to 1 mV s^{-1}.

Kinetic Analysis

- **Power law analysis: *b*-value determination**

  After recording a set of cyclic voltammograms at different scan rates, it was possible to perform the power-law analysis to determine the exponential *b*-value using the following relationship between the scanning rate (ν) and peak current (i_p).The peak current, i_p is proportional to the exponential of the scan rate and by plotting $\log(i_p)$ as a function of $log(\nu)$, *b*-value is determined as the slope of the linear fit.

  $$i_p = a \cdot \nu^b \quad \text{(Eq. 1)}$$

  $$\log(i_p) = \log(a) + b \cdot \log(\nu) \quad \text{(Eq. 2)}$$

  A *b*-value equal to 1 indicates a capacitive process, surface-limited, whereas b = 0.5 indicates a diffusion-limited process.

  Figure S34 illustrates the values obtained from both the cathodic and anodic b-values associated with both redox processes, which are summarized in Table S6.

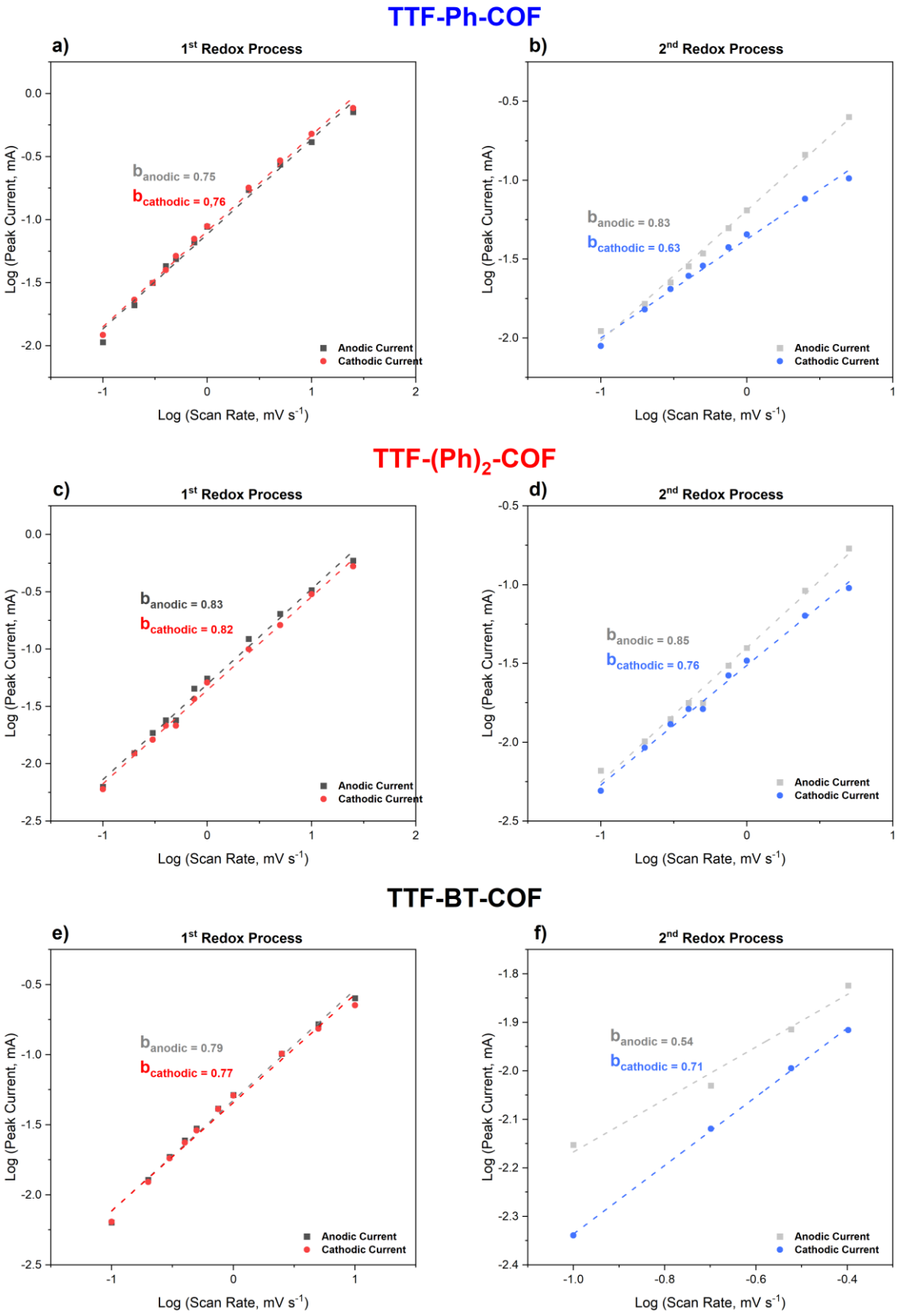

Figure S34. Power-law analysis for **TTF-Ph-COF**, **TTF-(Ph)$_2$-COF** and **TTF-BT-COF**. Linear plots of $\log(i_p)$ vs $\log(v)$ where the determined slope corresponds to the anodic and cathodic b-values for the two redox processes.

- **Dunn's Method**

The Dunn's method[23] was then used to further deconvolute the surface and bulk processes associated with the three COFs. At a fixed potential, the Dunn's method deconvolutes the capacitive and diffusion contributions following the equation:

$$i_p(V) = k_1 v + k_2 v^{0.5} \quad \text{(Eq. 3)}$$

$$\frac{i_p(V)}{v^{0.5}} = k_1 v^{0.5} + k_2 \quad \text{(Eq. 4)}$$

First, a set of potentials was fixed, between 2.5 V and 4.1 V at an interval of 0.05V (totaling 33 fixed potentials) and the measured current (i_p) associated with those fixed potentials at the different scan rates was determined. Afterwards, by plotting $i_p/v^{0.5}$ vs $v^{0.5}$ and applying a linear fit to the plot, it was possible to determine a set of k_1 and k_2 that were consequently used to determine the capacitive- and diffusion-controlled charge contributions by considering:

$$i_p(V) = k_1 v + k_2 v^{0.5} = i_{capacitive} + i_{diffusion} \quad \text{(Eq. 5)}$$

It is important to consider that, even though the capacitive and diffusion contributions were calculated and scan rates up to 1mV/s were used, this analysis is more valuable as a qualitative indicator due to the peak shift.

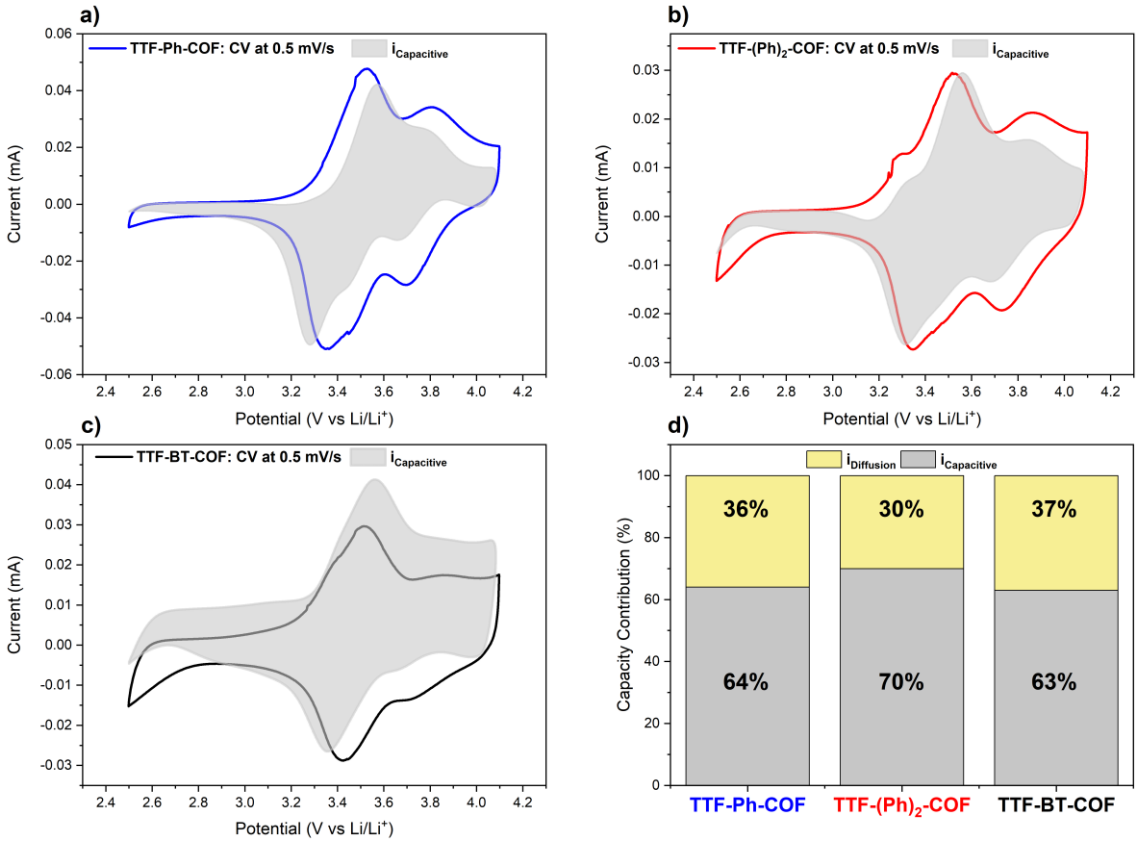

Figure S35. (a)-(c) Cyclic voltammograms of **TTF-Ph-COF**, **TTF-(Ph)$_2$-COF** and **TTF-BT-COF**, respectively, at 0.1 mV/s and the deconvoluted capacitive contributions shaded as gray area. (d) Calculated diffusion and capacitive contributions for each COF.

Table S6: Table summarizing the results obtained by the powers law and Dunn's method analysis.

		TTF-Ph-COF	TTF-Ph_2-COF	TTF-BT-COF
1st Redox Process	Anodic b-value	0.75	0.83	0.79
	Cathodic b-value	0.76	0.82	0.77
2nd Redox Process	Anodic b-value	0.83	0.85	0.54
	Cathodic b-value	0.63	0.76	0.71
% Capacitive		64 %	70 %	63 %
% Diffusion		36 %	30 %	37 %

Electrochemical impedance spectroscopy (EIS)

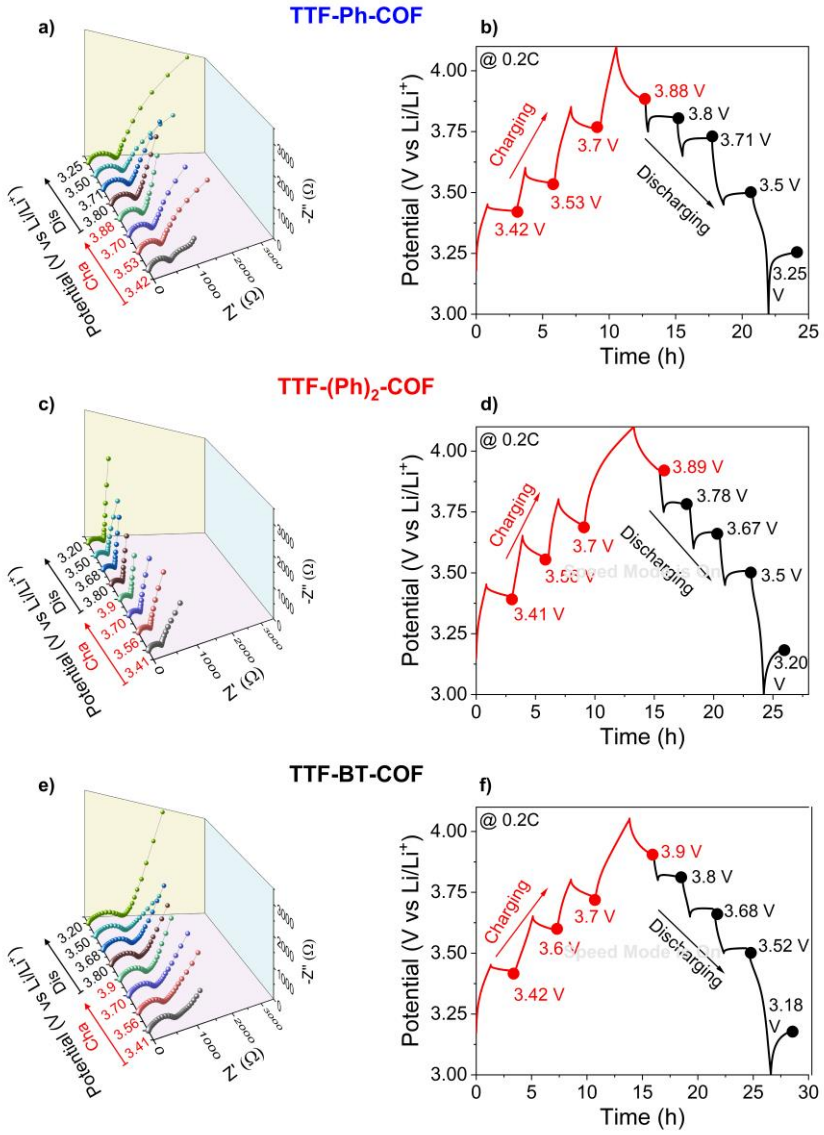

Figure S36. Electrochemical impedance spectroscopy (EIS) results obtained for **TTF-Ph-COF**, **TTF-(Ph)$_2$-COF** and **TTF-BT-COF** at different charging and discharging potentials.

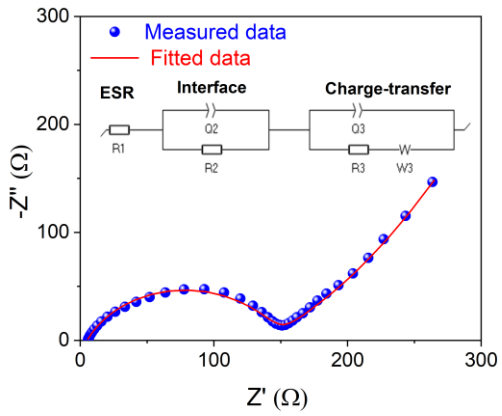

Figure S37. Equivalent circuit model for EIS data fitting.

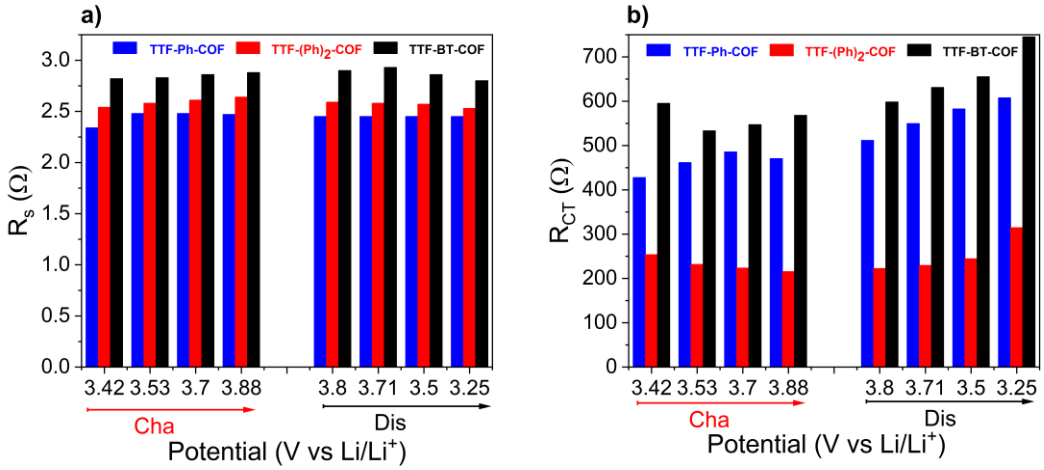

Figure S38. Comparative analysis of the equivalent series resistance (R_s) and charge-transfer resistances (R_{CT}) results obtained for **TTF-Ph-COF** (blue), **TTF-(Ph)$_2$-COF** (red) and **TTF-BT-COF** (black) at different charging and discharging potentials.

In general, R_s didn't experience huge variation at different state-of-charge and depth-of-discharges, i.e., during different charging and discharging potentials, respectively (Figure S38a). Additionally, the value of R_s was found to be lower for TTF-Ph-COF and TTF-(Ph)$_2$-COF compared to the TTF-BT-COF. Moreover, Ph-based COFs also experienced lower R_{CT} compared to the BT-COF (Figure S38b). Therefore, Ph-based COFs are expected to performance better capacitance performance (see below).

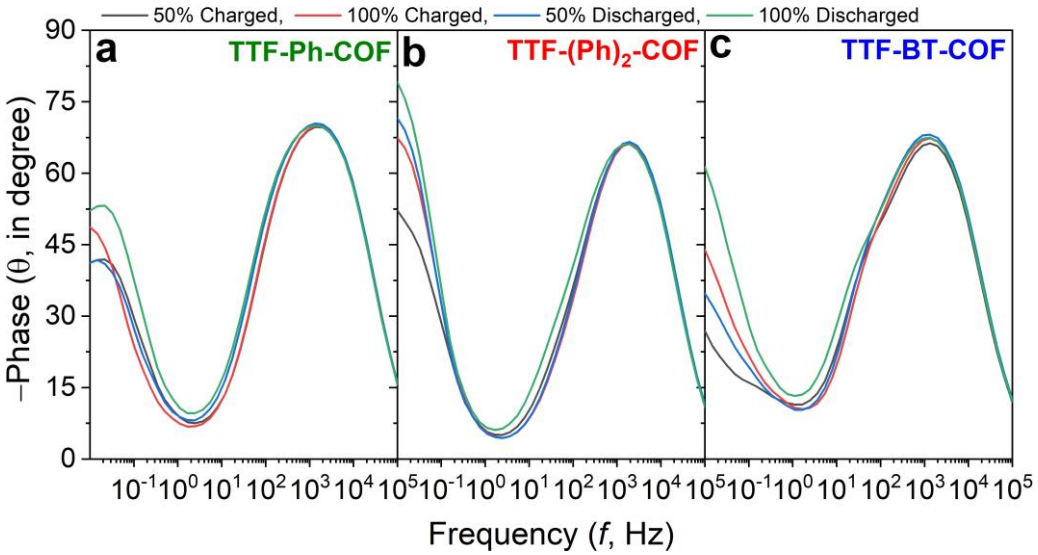

Figure S39. Phase angle obtained at 50 and 100% charged and at 50 and 100% discharged states obtained for a) **TTF-Ph-COF**, b) **TTF-(Ph)$_2$-COF** and c) **TTF-BT-COF.**

In general, the phase angle analyzed at 50 and100% charged and at 50 and 100% discharged states for TTF-Ph-COF and TTF-(Ph)$_2$-COF are higher than that for TTF-BT-COF. Therefore, faster charge storage mechanism is anticipated for Ph-based COFs than BT (see below).

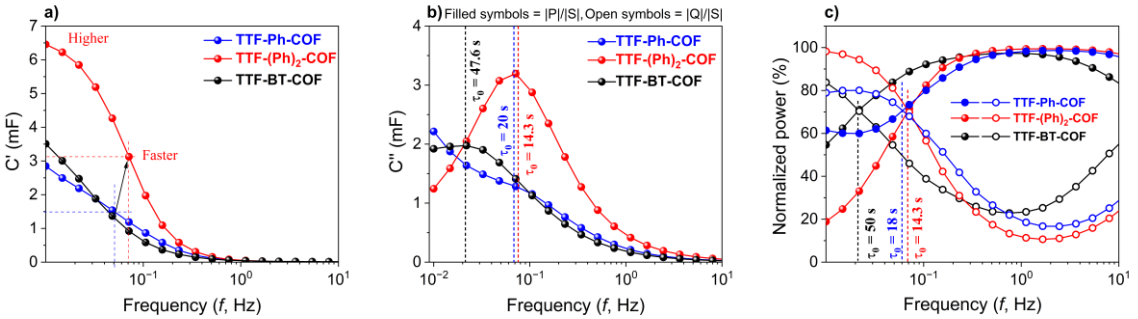

Figure S40. Real (a), imaginary (b) capacitance and characteristic time (c) analysis for **TTF-Ph-COF** (green), **TTF-(Ph)$_2$-COF** (red) and **TTF-BT-COF** (blue).

In general, lower R_s and R_{CT} leads to higher capacitance for TTF-(Ph)$_2$-COF (Figure S38), being in line with higher capacity utilization. Moreover, combination of lower resistances and higher capacitance dominance characteristics (high b-value and high surface-controlled charge storage contribution) render faster delivery of the stored charges, as witnessed by short characteristic time analysis in imaginary capacitance (Figure S40b) and complex power analysis (Figure S40c) plots for Ph-based COFs. Therefore, TTF-BT-COF exhibited relatively poor rate performance.

Galvanostatic intermittent titration technique (GITT)

The Galvanostatic intermittent titration technique (GITT) was performed by applying a series of current pulses that were then followed by a time where no current is used, denominated relaxation time. The GITT data was then used to determine the diffusion coefficients of the PF_6^- anion, both during the charging and discharging process.

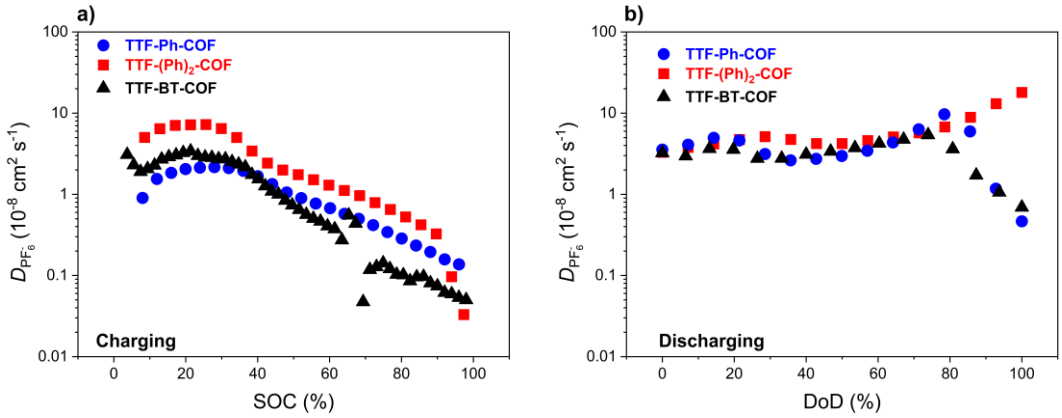

Figure S41. Diffusion coefficients of the PF_6^- anion for **TTF-Ph-COF** (blue), **TTF-(Ph)$_2$-COF** (red) and **TTF-BT-COF** (black) for charging (a) and discharging (b).

Even though differences are small, the performance according to the diffusivity of PF_6^- ions followed this order:

TTF-(Ph)$_2$-COF > TTF-Ph-COF > TTF-BT-COF

Overall, from both the Electrochemical impedance spectroscopy (EIS) and the Galvanostatic intermittent titration technique (GITT) indicate that:

TTF-(Ph)$_2$-COF > TTF-Ph-COF > TTF-BT-COF

Limiting to one-electron redox process

TTF-Ph-COF was tested in the full potential window of 2.5-4 V for the two-electron TTF-process and compared to a limited window of 2.5-3.6V to observe the charge and discharge behavior of the electrode when restricted to just the first one-electron process.

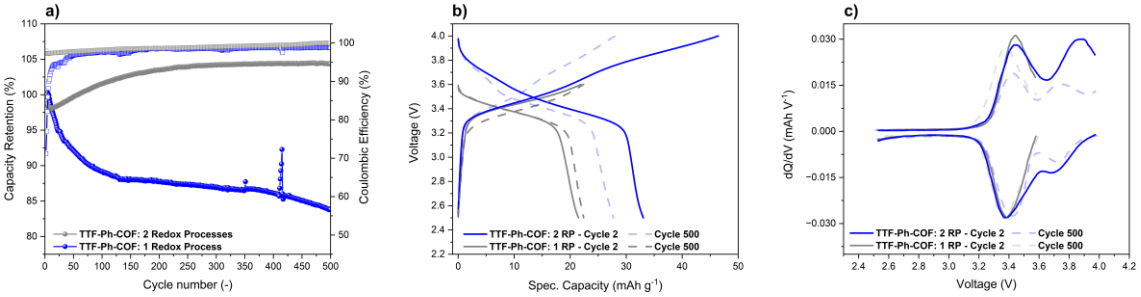

Figure S42. Galvanostatic charge–discharge (GCD) long cycling experiments of **TTF-Ph-COF** at 2C, using a potential window of 2.5-4V for the complete two-electron redox process (2RP) in blue, and a narrow window of 2.5-3.6V to the limited one-electron redox process (1RP) in grey.

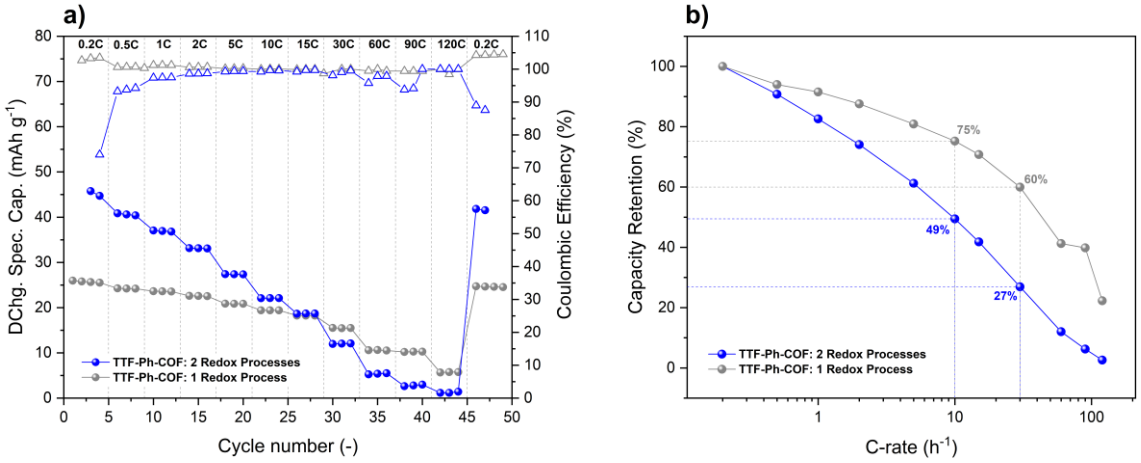

Figure S43. a) Rate capability performance of **TTF-Ph-COF** as a function of cycle number using a potential window of 2.5-4V for the complete two-electron redox process (2RP) in blue and a narrow window of 2.5-3.6V to the limited one-electron redox process (1RP) in grey. a) Gravimetric specific capacity versus C-rate. b) Capacity retention as a function of C-rate.

8. References

(1) Osterrieth, J. W. M.; Rampersad, J.; Madden, D.; Rampal, N.; Skoric, L.; Connolly, B.; Allendorf, M. D.; Stavila, V.; Snider, J. L.; Ameloot, R.; Marreiros, J.; Ania, C.; Azevedo, D.; Vilarrasa-Garcia, E.; Santos, B. F.; Bu, X.; Chang, Z.; Bunzen, H.; Champness, N. R.; Griffin, S. L.; Chen, B.; Lin, R.; Coasne, B.; Cohen, S.; Moreton, J. C.; Colón, Y. J.; Chen, L.; Clowes, R.; Coudert, F.; Cui, Y.; Hou, B.; D'Alessandro, D. M.; Doheny, P. W.; Dincă, M.; Sun, C.; Doonan, C.; Huxley, M. T.; Evans, J. D.; Falcaro, P.; Ricco, R.; Farha, O.; Idrees, K. B.; Islamoglu, T.; Feng, P.; Yang, H.; Forgan, R. S.; Bara, D.; Furukawa, S.; Sanchez, E.; Gascon, J.; Telalović, S.; Ghosh, S. K.; Mukherjee, S.; Hill, M. R.; Sadiq, M. M.; Horcajada, P.; Salcedo-Abraira, P.; Kaneko, K.; Kukobat, R.; Kenvin, J.; Keskin, S.; Kitagawa, S.; Otake, K.; Lively, R. P.; DeWitt, S. J. A.; Llewellyn, P.; Lotsch, B. V.; Emmerling, S. T.; Pütz, A. M.; Martí-Gastaldo, C.; Padial, N. M.; García-Martínez, J.; Linares, N.; Maspoch, D.; Suárez del Pino, J. A.; Moghadam, P.; Oktavian, R.; Morris, R. E.; Wheatley, P. S.; Navarro, J.; Petit, C.; Danaci, D.; Rosseinsky, M. J.; Katsoulidis, A. P.; Schröder, M.; Han, X.; Yang, S.; Serre, C.; Mouchaham, G.; Sholl, D. S.; Thyagarajan, R.; Siderius, D.; Snurr, R. Q.; Goncalves, R. B.; Telfer, S.; Lee, S. J.; Ting, V. P.; Rowlandson, J. L.; Uemura, T.; Iiyuka, T.; van der Veen, M. A.; Rega, D.; Van Speybroeck, V.; Rogge, S. M. J.; Lamaire, A.; Walton, K. S.; Bingel, L. W.; Wuttke, S.; Andreo, J.; Yaghi, O.; Zhang, B.; Yavuz, C. T.; Nguyen, T. S.; Zamora, F.; Montoro, C.; Zhou, H.; Kirchon, A.; Fairen-Jimenez, D. How Reproducible Are Surface Areas Calculated from the BET Equation? *Adv. Mater.* **2022**, *34,* 2201502. https://doi.org/10.1002/adma.202201502.

(2) Ding, H.; Li, Y.; Hu, H.; Sun, Y.; Wang, J.; Wang, C.; Wang, C.; Zhang, G.; Wang, B.; Xu, W.; Zhang, D. A Tetrathiafulvalene-Based Electroactive Covalent Organic Framework. *Chem. Eur. J.* **2014**, *20*, 14614–14618. https://doi.org/10.1002/chem.201405330.

(3) Cai, S. L.; Zhang, Y. B.; Pun, A. B.; He, B.; Yang, J.; Toma, F. M.; Sharp, I. D.; Yaghi, O. M.; Fan, J.; Zheng, S. R.; Zhang, W. G.; Liu, Y. Tunable Electrical Conductivity in Oriented Thin Films of Tetrathiafulvalene-Based Covalent Organic Framework. *Chem. Sci.* **2014**, *5*, 4693–4700. https://doi.org/10.1039/c4sc02593h.

(4) Jin, S.; Sakurai, T.; Kowalczyk, T.; Dalapati, S.; Xu, F.; Wei, H.; Chen, X.; Gao, J.; Seki, S.; Irle, S.; Jiang, D. Two-Dimensional Tetrathiafulvalene Covalent Organic Frameworks: Towards Latticed Conductive Organic Salts. *Chem. Eur. J.* **2014**, *20*, 14608–14613. https://doi.org/10.1002/chem.201402844.

(5) Caldeweyher, E.; Bannwarth, C.; Grimme, S. Extension of the D3 Dispersion Coefficient Model. *J. Chem. Phys.* **2017**, *147*. https://doi.org/10.1063/1.4993215.

(6) Caldeweyher, E.; Mewes, J.-M.; Ehlert, S.; Grimme, S. Extension and Evaluation of the D4 London-Dispersion Model for Periodic Systems. *Phys. Chem. Chem. Phys.* **2020**, *22*, 8499–8512. https://doi.org/10.1039/D0CP00502A.

(7) Caldeweyher, E.; Ehlert, S.; Hansen, A.; Neugebauer, H.; Spicher, S.; Bannwarth, C.; Grimme, S. A Generally Applicable Atomic-Charge Dependent London Dispersion Correction. *J. Chem. Phys.* **2019**, *150*, 154122. https://doi.org/10.1063/1.5090222.

(8) Aradi, B.; Hourahine, B.; Frauenheim, Th. DFTB+, a Sparse Matrix-Based Implementation of the DFTB Method. *J. Phys. Chem. A* **2007**, *111*, 5678–5684. https://doi.org/10.1021/jp070186p.

(9) Perdew, J. P.; Burke, K.; Ernzerhof, M. Generalized Gradient Approximation Made Simple. *Phys. Rev. Lett.* **1997**, *78*, 1396–1396. https://doi.org/10.1103/PhysRevLett.78.1396.

(10) Perdew, J. P.; Burke, K.; Ernzerhof, M. Generalized Gradient Approximation Made Simple. *Phys Rev Lett* **1996**, *77*, 3865–3868. https://doi.org/10.1103/PhysRevLett.77.3865.

(11) Tkatchenko, A.; DiStasio, R. A.; Car, R.; Scheffler, M. Accurate and Efficient Method for Many-Body van Der Waals Interactions. *Phys. Rev. Lett.* **2012**, *108*, 236402. https://doi.org/10.1103/PhysRevLett.108.236402.

(12) Ambrosetti, A.; Reilly, A. M.; DiStasio, R. A.; Tkatchenko, A. Long-Range Correlation Energy Calculated from Coupled Atomic Response Functions. *J. Chem. Phys.* **2014**, *140*. https://doi.org/10.1063/1.4865104.

(13) Blum, V.; Gehrke, R.; Hanke, F.; Havu, P.; Havu, V.; Ren, X.; Reuter, K.; Scheffler, M. Ab Initio Molecular Simulations with Numeric Atom-Centered Orbitals. *Comput. Phys. Commun.* **2009**, *180*, 2175–2196. https://doi.org/10.1016/j.cpc.2009.06.022.

(14) Marek, A.; Blum, V.; Johanni, R.; Havu, V.; Lang, B.; Auckenthaler, T.; Heinecke, A.; Bungartz, H.-J.; Lederer, H. The ELPA Library: Scalable Parallel Eigenvalue Solutions for Electronic Structure Theory and Computational Science. *Journal of Physics: Condensed Matter* **2014**, *26*, 213201. https://doi.org/10.1088/0953-8984/26/21/213201.

(15) Yu, V. W.; Corsetti, F.; García, A.; Huhn, W. P.; Jacquelin, M.; Jia, W.; Lange, B.; Lin, L.; Lu, J.; Mi, W.; Seifitokaldani, A.; Vázquez-Mayagoitia, Á.; Yang, C.; Yang, H.; Blum, V. ELSI: A Unified Software Interface for Kohn–Sham Electronic Structure Solvers. *Comput. Phys. Commun.* **2018**, *222*, 267–285. https://doi.org/10.1016/j.cpc.2017.09.007.

(16) Stephens, P. J.; Devlin, F. J.; Chabalowski, C. F.; Frisch, M. J. Ab Initio Calculation of Vibrational Absorption and Circular Dichroism Spectra Using Density Functional Force Fields. *J Phys Chem* **1994**, *98*, 11623–11627. https://doi.org/10.1021/j100096a001.

(17) Becke, A. D. A New Mixing of Hartree–Fock and Local Density-Functional Theories. *J Chem Phys* **1993**, *98*, 1372–1377. https://doi.org/10.1063/1.464304.

(18) Lee, C.; Yang, W.; Parr, R. G. Development of the Colle-Salvetti Correlation-Energy Formula into a Functional of the Electron Density. *Phys Rev B* **1988**, *37*, 785–789. https://doi.org/10.1103/PhysRevB.37.785.

(19) Vosko, S. H.; Wilk, L.; Nusair, M. Accurate Spin-Dependent Electron Liquid Correlation Energies for Local Spin Density Calculations: A Critical Analysis. *Can. J. Phys.* **1980**, *58*, 1200–1211. https://doi.org/10.1139/p80-159.

(20) Sarkisov, L.; Harrison, A. Computational Structure Characterisation Tools in Application to Ordered and Disordered Porous Materials. *Mol. Simul.* **2011**, *37*, 1248–1257. https://doi.org/10.1080/08927022.2011.592832.

(21) Sarkisov, L.; Bueno-Perez, R.; Sutharson, M.; Fairen-Jimenez, D. Materials Informatics with PoreBlazer v4.0 and the CSD MOF Database. *Chem. Mater.* **2020**, *32*, 9849–9867. https://doi.org/10.1021/acs.chemmater.0c03575.

(22) P. Pracht, F. Bohle, S. Grimme, *Phys. Chem. Chem. Phys.* **2020**, *22*, 7169–7192.

(23) Liu, T. C.; Pell, W. G.; Conway, B. E.; Roberson, S. L. *J. Electrochem. Soc.* **1998**, *145*, 1 882.